Proteasome hyperactivation rewires the proteome enhancing stress resistance, proteostasis, lipid metabolism and ERAD in *C. elegans.*

David Salcedo-Tacuma[1], Nadeeem. Asad[1], Giovanni Howells[1], Raymond Anderson[1], David M. Smith[1,2*]

1 Department of Biochemistry and Molecular Medicine, West Virginia University School of Medicine, 4 Medical Center Dr., Morgantown, WV USA
2 Department of Neuroscience, Rockefeller Neuroscience Institute, West Virginia University, Morgantown, West Virginia, USA
*Address correspondence to: David M. Smith, E-mail: dmsmith@hsc.wvu.edu.

Abstract

Proteasome dysfunction is implicated in the pathogenesis of neurodegenerative diseases and age-related proteinopathies. Using a *C. elegans* model, we demonstrate that 20S proteasome hyperactivation, facilitated by 20S gate-opening, accelerates the targeting of intrinsically disordered proteins. This leads to increased protein synthesis, extensive rewiring of the proteome and transcriptome, enhanced oxidative stress defense, accelerated lipid metabolism, and peroxisome proliferation. It also promotes ER-associated degradation (ERAD) of aggregation-prone proteins, such as alpha-1 antitrypsin (ATZ) and various lipoproteins. Notably, our results reveal that 20S proteasome hyperactivation suggests a novel role in ERAD with broad implications for proteostasis-related disorders, simultaneously affecting lipid homeostasis and peroxisome proliferation. Furthermore, the enhanced cellular capacity to mitigate proteostasis challenges, alongside unanticipated acceleration of lipid metabolism is expected to contribute to the longevity phenotype of this mutant. Remarkably, the mechanism of longevity induced by 20S gate opening appears unique, independent of known longevity and stress-resistance pathways. These results support the therapeutic potential of 20S proteasome activation in mitigating proteostasis-related disorders broadly and provide new insights into the complex interplay between proteasome activity, cellular health, and aging.

Introduction

Neurodegenerative diseases (NDs) and age-related proteinopathies, such as Alzheimer's and Parkinson's disease, pose a significant challenge to public health due to their devastating impact on the aging population. These disorders are characterized by the accumulation of misfolded proteins[1–7], particularly intrinsically disordered proteins (IDPs)[3,5,7], which lack stable three-dimensional structures and are prone to aggregation[1–7]. The accumulation of these toxic proteins leads to neuronal dysfunction and disease progression, implicating the role of the proteostasis network and the ubiquitin-proteasome system (UPS) in maintaining cellular health[1,2]. The proteostasis network is a complex and interconnected system that maintains cellular protein homeostasis through the coordination of protein synthesis, folding, and degradation[1,8–10]. Molecular chaperones facilitate the folding of newly synthesized proteins, refold misfolded proteins, and prevent protein aggregation[8,10–12]. These chaperones work in concert with degradation pathways, such as autophagy, ERAD, and the UPS, to remove damaged or misfolded proteins and prevent the accumulation of proteotoxic species[8–10,12]. The proteostasis network also integrates stress response pathways, including the oxidative stress response, heat shock response (HSR), and unfolded protein response (UPR), which communicate stress indicators and allow the network to adapt to changing cellular conditions[13,14]. Disruptions to the proteostasis network can have far-reaching consequences,

contributing to the development and progression of various diseases, particularly those associated with aging[10,11,15].

The proteasome, a component of the UPS, plays a crucial role in protein quality control by degrading damaged and misfolded proteins. Impairment of proteasome function has been implicated in the pathogenesis of various neurodegenerative diseases, as evidenced by the presence of ubiquitinated protein aggregates in affected tissues[16–18]. Moreover, certain pathological oligomers, such as those derived from amyloid-β, α-synuclein and Huntingtin, have been shown to inhibit proteasome activity by allosterically affecting the opening of the 20S proteasome gate[19,20]. This highlights the importance of understanding the mechanisms that regulate proteasome function and the potential of targeting the proteasome for therapeutic intervention.

Enhancing proteasome activity emerges as a promising strategy for combating age-related proteinopathies. Studies have shown that increasing proteasome activity, either through genetic manipulation or pharmacological intervention, can improve the clearance of aggregation-prone proteins and alleviate disease phenotypes in various model systems. For example, specific HbYX motif peptides have been shown to facilitate and enhance the 20S proteasome ability to degrade IDPs, and reverse the inhibitory effects of toxic oligomers *in-vitro*[20–22]. Additionally, several drugs can influence the post-translational modifications (PTMs) of the 26S proteasome to induce activity *in-vivo*[23]. Even overexpression of some proteasome subunits, which can increase the levels of proteasome, can prove beneficial to the organism, extending their lifespan and providing resistance against stressors [23–28]. However, the complexity of the proteostasis network and the potential unintended consequences of modulating proteasome activity warrant careful consideration. It is crucial to understand the safe limits of proteostasis manipulation and the impact of proteasome activation on cellular function and organismal health, as the proteostasis network maintains a delicate equilibrium, and significant alterations in one component could disrupt this balance, leading to unforeseen effects on cellular regulation and homeostasis.

To address these questions and investigate the therapeutic potential of proteasome hyperactivation, we developed a *Caenorhabditis elegans* model with a hyperactive proteasome. This was done by using CRISPR-Cas9 to induce a truncation of the N-terminal domain of the α3 subunit (pas-3) of the 20S proteasome (α3ΔN-20S), which generates a constitutively open-gate 20S form[28]. *C. elegans* are a valuable model organism for studying aging and age-related diseases due to its short lifespan, ease of genetic manipulation, and conservation of key molecular pathways. The initial characterization of this "open-gate" mutant (α3ΔN) revealed significant benefits for the organism's biology, including increased 20S peptidase activity, lifespan extension, and resistance to heat shock[28], suggesting an improved capacity to maintain proteostasis. The α3ΔN mutant's hyperactivation implies continuous operation beyond the usual regulated activity, potentially affecting the typical degradation rates of some proteins, especially nascent and IDPs. The open 20S proteasome is highly capable of degrading IDPs since unfolded proteins can defuse into the opened 20S. In contrast, folded proteins typically require ubiquitination and targeting to the 26S proteasome (19S-20S), which can unfold and inject them into the 20S core[29,30]. As most pathological proteins that accumulate in neurodegenerative diseases are IDPs[31–36], the "20S pathway" for degradation becomes highly relevant in the context of the α3ΔN mutants hyperactivation.

In this study, we employ a multi-omics approach to elucidate the broad-spectrum impact of proteasome hyperactivation on the proteome and transcriptome in our *C. elegans* model. Our findings reveal a comprehensive rewiring of cellular pathways in response to enhanced proteasome activity, including increased protein synthesis, oxidative stress resistance, and changes in lipid homeostasis. We demonstrate that proteasome hyperactivation leads to the selective degradation of IDPs, which are known to play a critical role in the pathogenesis of neurodegenerative diseases. This accelerated targeting of IDPs highlights the potential of the hyperactive proteasome to alleviate the accumulation of toxic protein aggregates in these disorders. Furthermore, we uncover a novel role for the 20S proteasome in regulating ERAD, leading to the efficient clearance of aggregation-prone proteins such as ATZ, which accumulates in the liver in alpha-1 antitrypsin deficiency[37,38]. These findings underscore the therapeutic potential of proteasome hyperactivation in diseases associated with ERAD dysfunction and proteostasis imbalances.

Our results also shed light on the complex interplay between proteasome activity, cellular homeostasis, and organismal health. We observe a lipid reduction phenotype in the α3ΔN mutant, accompanied by increases in lipid droplet size and peroxisome proliferation. Lipid droplets have emerged as crucial players in cellular signaling, metabolic health, and neurodegenerative diseases, beyond their traditional role as mere storage organelles. We also identify splicing variations in the spastin gene, which may influence its role in lipid droplet-peroxisome dynamics, providing a potential link between proteasome activity and neuronal health. These findings highlight the potential of proteasome hyperactivation to modulate lipid metabolism and organelle dynamics in the context of age-related diseases, of which there are many.

Current therapeutic approaches for neurodegenerative diseases have limitations, emphasizing the need for novel strategies that target the underlying molecular mechanisms. The main objectives of this study are to elucidate the cellular and organismal adaptations to proteasome hyperactivation, investigate its potential as a therapeutic strategy for age-related proteinopathies and neurodegenerative disorders, and understand the safe limits of proteostasis manipulation for organismal health. By addressing these questions, we aim to provide novel insights into the molecular basis of aging and develop targeted interventions to promote healthier aging. Our findings highlight the therapeutic potential of stimulating 20S proteasome activity and its implications for proteostasis-related disorders, opening new avenues for the development of targeted therapies for age-related proteinopathies and neurodegenerative diseases.

Results:

Proteome rewiring in the open gate mutant.

The first step was to assess the proteomic changes in the open gate proteasome mutant α3ΔN using Tandem Mass Tag-mass spectrometry (TMT-MS). Our focus was on 8-day old adult worms (n=5), a stage marking the onset of age-related phenotypes and detectable age-related proteomic and transcriptomic signatures[11,39,40]. Proteins from MS were identified and matched against the *C. elegans* protein database using MaxQuant software[41]. This analysis yielded 52,000 peptides corresponding to 4,267 proteins (*Q-value<0.01*). Normalization and variance quantification of protein expression (FigS1), followed by unsupervised hierarchical clustering and Principal Component Analysis (PCA), revealed distinct proteome profiles between the open gate mutant and wild type, affirming the reproducibility of our experimental replicates (Fig 1A). Utilizing DEqMS[42], a

method offering enhanced sensitivity and specificity for proteomic data, we identified 459 differentially expressed proteins (DEPs) (FDR<0.05 and $Log_2FC>|0.59|$, TableS1), representing approximately 10% of the total protein expression profile. Specifically, we observed 252 downregulated and 207 upregulated proteins in the α3ΔN open gate mutant (Fig 1B). Notably, no significant changes were detected in the expression of the 20S proteasomal subunits pas 1-7 and pbs 1-7 (FigS2B-C, and previously demonstrated by PAGE *(Anderson et. Al.*[28]*)*), confirming that the increased proteasomal activity is attributed to the open gate modification rather than changes in proteasome abundance.

Next, to elucidate the biological significance of these changes from the proteome profile, we performed Gene Set Enrichment Analysis (GSEA)[43]. The analysis identified two primary functional groups affected by proteasome hyperactivation: increased protein quality control (e.g. ribosome biogenesis and mRNA processing factors), and decrease in lipid metabolism (Fig1C). We discovered a notable enrichment in processes related to translational activity, including ribosome biogenesis, RNA-Binding Proteins (RBPs), and RNA processing. In normal physiological conditions, the proteasome-mediated degradation of RNA binding proteins, which are enriched in intrinsic disorder regions (IDRs), serves as a critical regulatory process. This is essential for maintaining appropriate protein levels for vital cellular functions such as gene expression, DNA repair, and RNA processing[44–46]. The observed upregulation of these proteins in the α3ΔN mutants suggests a selective degradation pressure on these substrates, which the organism compensates for by upregulating these critical proteins to excessive levels in order to preserve these vital functions. If 90% of these highly susceptible proteins are degraded before they had the opportunity to carry out their normal function, then the cell would need 10X more than normal. This scenario aligns with the hypothesis that enhanced degradation, facilitated by the α3ΔN open gate 20S, leads to a rapid turnover of certain proteins.

Interestingly, the proteins involved in ribosome biogenesis, RBPs, and RNA processing are predominantly poorly characterized in *C. elegans*, some are linked to splicing and RNA binding activities that activate both the Unfolded Protein Response (UPR) and mitochondrial UPR[11,47]. Alongside ribosome complex formation, mitochondrial ribosomal subunits mrpl-24 and mrpl-41 showed elevated levels (Table S1), indicating enhanced protein synthesis. Downregulation of these two ribosomal subunits has been linked to negative impacts on lifespan and stress resistance, as evidenced by studies of mutants with mRNA processing defects[11,48,49]. Moreover, cytosolic ribosomal proteins and overall protein synthesis decrease with age in *C. elegans*[11].

In addition, the increased expression detected in RBPs, cytosolic ribosomal subunits, and splicing factors, revealed by the proteomics, suggests a significant reconfiguration of the translation machinery. This reconfiguration potentially drives a higher rate of protein synthesis, following 20S proteasome gate-opening. To test this hypothesis, we employed a technique to label newly synthesized proteins in live worms using 6-FAM-puromycin, a fluorescently tagged version of puromycin that integrates into nascent polypeptide chains, thereby marking newly formed proteins[50]. The fluorescence intensity of 6-FAM-puromycin incorporation serves as an indicator of protein synthesis rates. To ensure the accuracy of our measurements, we normalized the fluorescence signals to those obtained from worms treated with cycloheximide, a well-known inhibitor of protein biosynthesis. This comparison allows for the quantification of protein synthesis

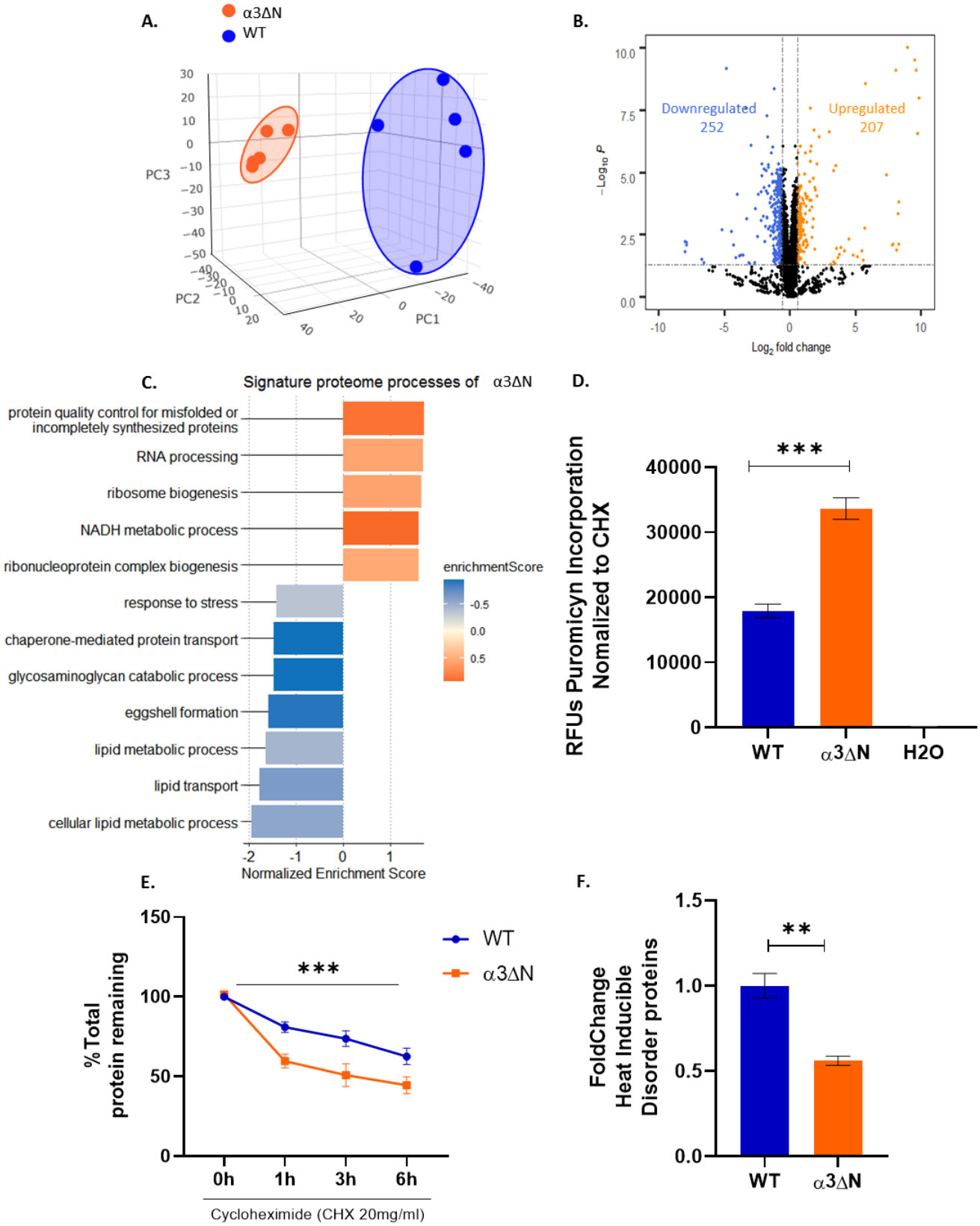

Figure 1. Open gate mutant α3ΔN rewires the proteome of *C. elegans decreasing disorder* proteins and increasing global synthesis: A) Dimensionality reduction via three-dimensional PCA was performed on TMT-MS data to depict profile differences between n=5 wild-type (WT) and α3ΔN mutants. **B,** Volcano plot of Differentially Expressed Proteins (DEPs) detected Log2FC α3ΔN/WT vs - log10FDR. All points above the dotted line are statistically significant (FDR<0.05). Blue points above the x axis dotted line represent DEPs downregulated (FC<-1.5) and orange dots represent DEPs upregulated (FC>1.5). **C.** GSEA of DEPs found in α3ΔN mutants, x axis represents the Normalized enriched score for each of the categories according to ClusterProfiler in R; FDR<0.05. **D.** Rates of protein translation in live *C.elegans* determined by 6-FAM-puromycin, lysing and, separating free 6-FAM-puro from labeled nascent proteins with desalting columns, following by fluorescent quantification in plate reader. Bars represent mean +/-SEM of n=6, ****p<0.01 ordinary One-way-ANOVA*. **E.** CHX assay to assess global protein degradation rates over 6 h of CHX or CHX+MG132 treatments in α3ΔN mutants. CHX/MG132 ratios were normalized to the 0h timepoint of the respective strain. Values are depicted as mean ± SEM generated from *n* = 3 independent experiments. Statistical significance was determined using Satterthwaite's degrees of freedom method with ImerTest, ***p<0.001 indicating a statistically significant difference between conditions. **F.** Quantification of intrinsically Disorder Proteins (IDPs) content in WT and α3ΔN mutants. IDPs from lysates were enriched by two steps of heat denaturation and precipitation of folded proteins, leaving primarily IDPs. SDS-page gels were quantified after commassie staining. Bars represent means +/-SEM. n=3, ***p<0.01 unpaired t-test.*

rates by measuring the relative increase or decrease in the incorporation of 6-FAM-puromycin into proteins. We observed a nearly 2-fold increase in protein synthesis in the α3ΔN strain (Fig1D). This result validates the GSEA enrichment analysis from the TMT-MS data, particularly in the areas of ribosomal biogenesis, mRNA processing, and RBP signaling, highlighting their integral involvement in boosting protein synthesis. This acceleration in synthesis is likely crucial for sustaining proteome stability in the face of accelerated degradation by the α3ΔN strain illustrating a sophisticated mechanism by which cells adapt to ensure continued function during the increased protein turnover. To confirm that α3ΔN had enhanced protein degradation *in-vivo*, we blocked protein synthesis with cycloheximide and measured the decrease of total protein levels by SDS-gel with or without a proteasome inhibitor. We observed that the α3ΔN strain degraded proteins more rapidly than WT (Fig 1E). The simultaneous acceleration of protein degradation and protein synthesis supports the hypothesis that enhanced protein synthesis is likely an adaptive response to balance out proteasome hyperactivation to maintain proteome stability.

We next investigated the impact of the hyperactive proteasome on intrinsically disordered proteins (IDPs), which can be degraded by the 20S in a ubiquitin-independent manner [31,44,51]. Our analysis, (Fig 1F), showed a remarkable 50% reduction in heat stable protein levels—which are primarily IDPs[52] — in the open gate mutant, indicating an accelerated degradation of these proteins. To ask if the acceleration of global protein degradation in the α3ΔN was primarily due to IDP degradation we correlated the protein levels from MS data with protein disordered content. However, analysis of the mass spectrometry data showed no significant correlation between protein structure/disorder and the change in detected protein levels. (Fig S1E). Given their rapid targeting and degradation by the hyperactive proteasome, or the overcompensation in expression of highly susceptible but functionally critical proteins, our mass spectrometry dataset may exhibit a certain degree of detection bias, complicating such analysis. Therefore, while it's clear that global protein degradation and IDP degradation are accelerated in α3ΔN, it is unclear what the differential effects are on the complete spectrum of protein disorder.

Transcriptomic profile of open gate mutants

Given the observed differences in mRNA processes, RNA binding proteins, and translation in our study, we hypothesized significant changes in the transcriptomic profiles of the open gate mutants. To investigate this, we conducted RNA sequencing on 8-day-old adult worms (n=5). The PCA (Fig 2A), revealed a distinct separation between the open gate mutant and wild type strain profiles, indicating different global expression programs. This finding was consistent with the changes observed in the proteome, confirming our hypothesis of fundamental rewiring due to proteasome hyperactivity. Using DESEQ2.0[53], we identified 1,756 differentially expressed genes (DEGs) in the open gate mutant, with 854 genes upregulated and 902 downregulated (Fig 2B-FigS2A, TableS2). Notably, the expression of key proteasome subunits (FigS2B-C) and related transcription factors, such as NRF2 and SKN1, (TableS2) were not significantly affected by 20S gate-opening. The correlation between protein and transcript levels changes caused by the hyperactive proteasome was modest (R^2 = 0.45. Fig 2C) indicating that post-translational mechanisms are primarily responsible for their differential expression. Interestingly, both omics datasets showed similar enrichment patterns in stress response and lipid metabolism (FigS1F-FigS2D). Additionally, consistent changes in proteostasis components, such as UPR, oxidative stress defense, and small heat shock proteins, were observed across both datasets, indicating synchronized impacts on synthesis and degradation control networks (Fig 2D,E; Hypergeometric distribution FDR<0.05).

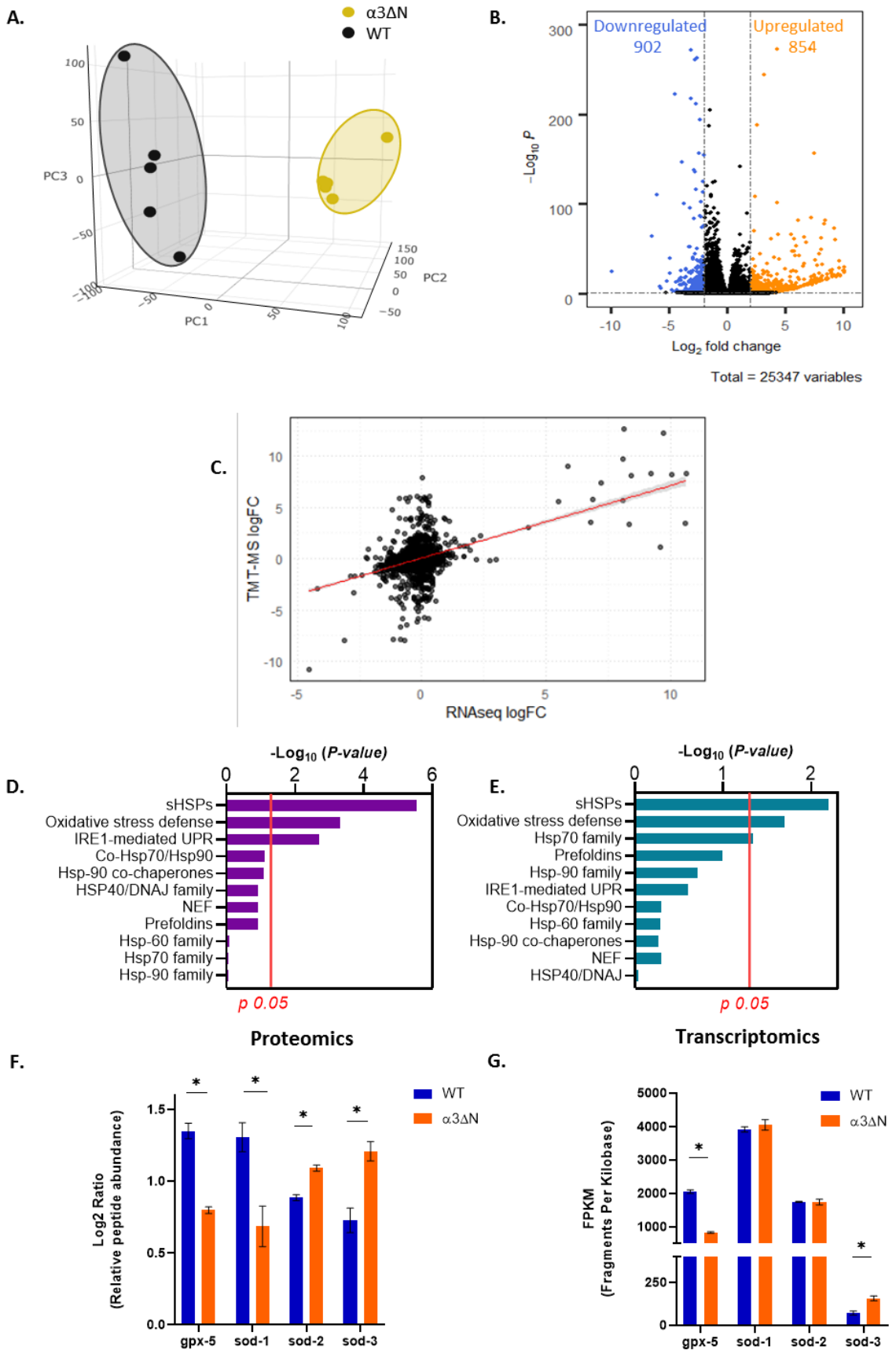

Figure 2. Open gate mutant α3ΔN impacts the transcriptome of proteostasis components involved in oxidative stress defense. A. Three Dimensional PCA of RNA-seq data to depict differences in the expression profile of WT and α3ΔN mutants (n=5). **B,** Volcano plot of Differentially Expressed Genes (DEGs) detected Log2FC α3ΔN/WT vs - log10FDR. All points above the dotted line are statistically significant (FDR<0.05). Blue points above the x axis dotted line represent DEGs downregulated (FC<-2) and orange dots represent DEGs upregulated (FC>2). **C.** Scatter plot comparing relationship between protein (y axis TMT-MS log2FC) and transcript levels changes (RNAseq log2FC). Red line represents the best fit for regression. Pearson correlation coefficient R=0.45, *p<0.05.* **D-E.** Enrichment Analysis of Proteostasis Network Components in Proteomics (D) and Transcriptomics (E) data. Statistical significance was assessed using the Hypergeometric Distribution, with *adjusted p-value* of <0.05 indicating significant enrichment. The x-axis indicates the –log10(*p*-value) and red line indicates a threshold of *adj-p* = 0.05 [–log10(0.05) =1.3]. **F-G.** Quantitative Expression of Oxidative Stress Response Genes in α3ΔN Mutants. Panel F depicts the log2 relative protein abundance, while Panel G illustrates the gene expression measured in FPKM. Data are presented as mean ± SEM. Genes marked with an asterisk (*) denote significant differential expression found in each analysis (FDR< 0.05).

Specifically, alterations in BIP homologs hsp-4, hsp-3, small heat shock proteins, and downregulation of transcription factor BTF3 homolog ICD1, involved in UPR, were notable (Fig 2D,E; TableS1). Enhanced oxidative stress defense was enriched through increase of mitochondrial SOD-2 and SOD-3 and a decrease in cytoplasmic SOD-1, which is known to influence lifespan in *C. elegans*[54,55] (Fig 2F,G). The reduction of cytoplasmic SOD-1 and glutathione peroxidases gpx-5 in the α3ΔN strain indicate a reduced requirement for oxidative stress defense in the cytoplasm.

In addition, several small heat shock proteins (sHSPs) were also downregulated (TableS1), which are the first responders to protein misfolding, indicating that 20S gate opening in α3ΔN leads to more efficient elimination of oxidized or damaged proteins[11] generating a cellular environment with reduced need for proteostasis machinery. We next sought to test this hypothesis.

Hyperactivation of the proteasome increases the oxidative stress defense of *C.elegans.*

The observed alterations in the proteostasis network prompted us to investigate the open gate mutant's stress response capabilities. Previous studies have shown that this model exhibits resistance to paraquat[28], a compound known for generating mitochondrial reactive oxygen species (ROS) and inducing apoptosis. However, the specific mechanisms by which proteasome hyperactivation confers this resistance remained elusive. First, to determine if oxidative damage is reduced in the α3ΔN strain, we explored post-translational modifications (PTMs) focusing on oxidation-induced modifications in our TMT dataset. In our analysis, we identified 1,997 peptides exhibiting signs of oxidative modifications. Among these, 63 showed a significant decrease in oxidation levels, while 22 were found to be upregulated (Fig3A). The observed increase in oxidation on certain peptides suggests a potential for damage to the proteins. Notably, this includes significant alterations to proteins such as the major sperm protein, Y59E9AR.7, an observation that aligns with previously reported fertility challenges [28] (TableS3). Conversely, the reduction in oxidative markers on other peptides may imply enhanced protein stability[44], a decrease in oxidative stress within the open gate mutant, or increased degradation of oxidatively damaged proteins. This phenomenon could be indicative of a more robust and less damaged proteome, particularly in the context of aging worms, which we hypothesized confers an increased resistance against oxidative stress damage. To confirm the increase in oxidative stress defense, we subjected the open gate mutants to acute oxidative stress using various compounds that induce Reactive Oxygen Species (ROS) in the cytosol and the mitochondria, including H_2O_2 which is particularly relevant for *C. elegans*, as it is produced by pathogenic bacteria in their natural environment[56,57]. We also used tert-butyl hydroperoxide (tBoOH), another cytosolic ROS generator with greater stability than H_2O_2[58]. We also employed Aldicarb, an acetylcholinesterase inhibitor which is used for synaptic transmission assessment[59] as well as juglone, a mitochondrial stressor known to induce ROS through the activation of the FLP neuropeptide family, causing mitochondrial stress[60]. Additionally, to understand the role of Superoxide Dismutases (SODs) in this response, we crossed the open gate mutants with the MQ1766 strain, which lacks all SOD genes and is known to be sensitive to oxidative stressors[55]. Our results revealed that α3ΔN open gate mutants display a markedly enhanced resistance to oxidative stressors H_2O_2, tBoOH, and juglone (Fig 3B-D), while their response to the neurotoxic agent aldicarb remains unchanged (FigS3A), as it functions via a non-ROS mechanism.

Through probit curve analysis, we quantified the lethal dose 50 (LD50) and resistance ratios (RR) for each of these compounds(FigS3B-E). The analysis indicates that a 3.43-fold higher concentration of H_2O_2 is required to affect 50% of the open gate mutant population(FigS3B,E).

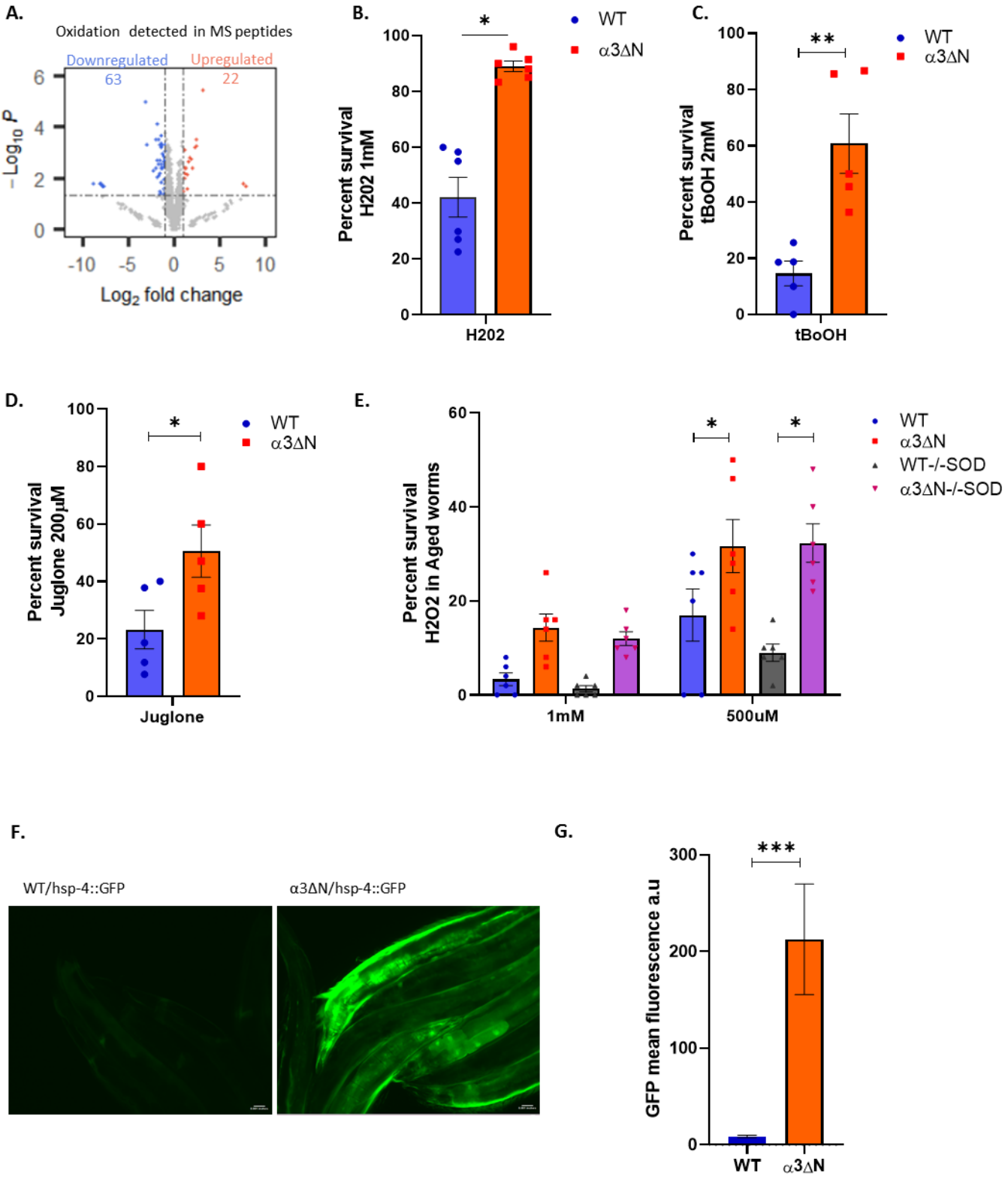

Figure 3. Enhanced Oxidative Stress Resistance in open gate mutants α3ΔN. A. Volcano plot of the differentially post-translation modified (PTM) oxidated peptides detected in the TMT-MS with Maxquant *(Q<0.01).* Blue points above the x axis dotted line represent oxidated peptides downregulated (FC<-1.5) and yellow dots represent oxidated peptides upregulated (FC>1.5). Distribution of peptides was adjusted with Limma model and significance was determined with ANOVA and Tukey correction for multiple test*(FDR<0.05)*. **B-D.** Percentage of surviving of WT and α3ΔN, 1 day adult worms after acute oxidative stress challenge with H2O2 at 1mM (B), tBoOH at 2mM (C) and juglone at 200µM (D). Data represents mean values ± SEM of at least three independent experiments $*p < 0.05$, $**p < 0.01$ by unpaired two-tailed *t*-test. **E.** Percentage of surviving old age worms (Day 8) of the indicated genotypes after acute oxidative stress challenge with H2O2 at 1mM and 500 µM. WT-/-SODs, knockout worms for SODs and α3ΔN-/-SODs indicates open gate worms crossed into -/-SODs knockout strain. Data represents mean values ± SEM of at least three independent experiments $*p < 0.05$ by two-way-ANOVA with Sidaks correction for multiple comparisons-test. Representative images (**F**) and fluorescent quantification (**G**) of WT/hsp-4::GFP and α3ΔN/hsp-4::GFP transgenic worms expressing the oxidative stress reporter hsp-4::GFP. Zoomed-in images of the worms at 20x. Scale bar, 25 µm. Data in G represents mean values ± SEM of at least three independent experiments $***p < 0.01$ two-tailed *t*-test.

Similarly, the mutants require a 4.25-fold increase in the concentration of tBoOH (FigS3C,E) and a 1.84-fold increase for juglone to reach the LD50 threshold (FigS3D,E). Intriguingly, crossing the α3ΔN open gate mutants with the SOD-deficient strain resulted in a diminished stress resistance overall relative to the WT. However, their capacity to withstand tBoOH and H_2O_2 stress was not only preserved but also remained notably effective into advanced age, emphasizing a partial but significant retention of resilience, even without protective SOD enzymes (Fig3E-FigS3E). The one exception was Juglone, which exhibited similar toxicity in SOD-/- worms regardless of the α3ΔN mutation. This could be expected since juglone causes mitochondrial ROS, and mitochondria don't contain proteasomes. The consistent resistance of α3ΔN to H_2O_2 in older worms emphasizes the presence of a durable system capable at handling protein damage across the lifespan of *C. elegans* (Fig3E). This observation, in addition to the changes in heat shock proteins from the omics data, led us to hypothesize that α3ΔN has an inherent increase in the stress response capacity, enhancing their resilience to various stressors, even into old age.

To directly assess activation of stress pathways in our strain we crossed it with two reporter strains. 1)SJ4005, which expresses hsp-4::GFP, serving as a marker for the UPR through its homology to the ER chaperone BiP [61]. 2) GL347, expressing hsp-6p::GFP, which acts as an indicator of mitochondrial UPR induction (mtUPR)[62]. Our results showed that there were no changes in mtUPR response in the α3ΔN strain relative to WT as measured by hsp-6p::GFP fluorescence (FigS3F), indicating that the mitochondria were not stressed. Interestingly, under normal conditions the open gate strain crossed with hsp-4::GFP reporter showed a marked increase in fluorescence(Fig3F,G). These findings indicate an inherently elevated stress response in the ER, potentially activated through the unfolded protein response (UPR) pathway. The elevation in hsp-4::GFP is often associated with changes in expression when various heat shock proteins (hsps) are downregulated[63,64], a finding that aligns with our omics data, which reported a downregulation in crt-1 and several HSPs such as hsp-3,hsp-4 and small heat shock hsp-16.1, hsp-16.48, and hsp-16.49 (Table S1 and Table S2). However, we don't fully understand the reason behind the increased UPR hsp-4 reporter. We interpret the observed upregulation in the UPR within the α3ΔN strain as a consequence of enhanced clearance of oxidatively damaged proteins, rather than a direct result of increased ER stress. Notably, we also did not detect any change in XBP1 splicing, a recognized indicator of UPR activation, suggesting that at least this particular pathway of the UPR is not activated (Fig S2E). This implies that the overall UPR activation observed may not be attributed to enhanced ER stress. Alternatively, the open gate mutant could be causing ER stress that upregulates UPR, however, we test this below and find the opposite (Fig5E). This activation pattern in the UPR further bolsters the mutant's enhanced capability to preemptively counteract stress, even ER stress, highlighting the integral role of these pathways in supporting the organism's resilience against environmental challenges.

Open gate mutants and lipid homeostasis

The omics data revealed significant alterations in lipid metabolism and transport in the open gate mutant worms, marking a major aspect of expression remodeling. This includes the reduced expression of 56 proteins integral to lipid homeostasis, such as the long fatty acid transporter pmp-2 and the lipid-binding protein NRF-5, a homolog of mammalian secreted lipid-binding proteins. In contrast we also observed upregulation of key enzymes involved in lipid catabolism including: Acyl-CoA synthetase 3 (acs-3), and acyl-CoA dehydrogenase 8 (acdh-8) (TableS1). These two enzymes work sequentially in the fatty acid β-oxidation pathway to break down fatty acids and generate

acetyl-CoA for energy production. acs-3 activates fatty acids for entry into the pathway and acdh-8 performs the first oxidation step[65,66].These metabolic alterations affect a range of processes from cellular energy homeostasis to lipid droplet (LD) biogenesis, indicating a profound remodeling of lipid metabolism in the mutant.

To validate these findings, we first assessed the lipid content in our open gate mutant worms using Oil Red O staining. We observed a notable depletion of lipids, Oil red O staining of α3ΔN worms was reduced by 52% *(p <0*.01) aligning with the predicted downregulation of lipid metabolic enzymes in the omics data (Fig 4A,B). Next, we confirmed the reduction in LDs with two different approaches. The first approach was to perform vital staining of lipid droplets in live worms with BODIPY, a dye that binds to lipid droplets[67]. We found a significant reduction in the number of LDs and significant increase in the size of the LDs (Fig4C-D), supporting the observed lipid depletion phenotype (Fig 4A,B) and impacts in LDs. To bolster these results, we took an orthogonal approach and crossed our open gate mutant into the ABR339 strain which contains endogenous lpin-1 fused to GFP, a homolog of LIPIN1, which is important for the ER membrane LD biogenesis, bud formation[68–71] and works effectively as a LD marker as proven by the co-staining in LD with Nile red (FigS4A). In agreement with the BODIPY, we found significant decrease in the number of LDs and significant increase in size (Fig4E-F).

To complement our understanding of LDs remodeling in the open gate mutants, we looked into the sub-organelles, peroxisomes, which are tightly linked to LDs[68,72]. Peroxisomes not only play a pivotal role in the catabolism of long-chain and very-long-chain fatty acids, but also participate in the dynamics and composition of LDs through their involvement in the metabolism of specific lipid species that can be associated with LDs[68,72,73]. Additionally, peroxisomes are directly involved in the biosynthesis of plasmalogens, critical phospholipids for the structure and function of cellular membranes[72,74]. For this, we crossed the open gate mutant into the WBM1177 strain which contains a GFP fused to a peroxisome localization sequence (SKL) eft-3p::GFP–SKL[68]. Surprisingly, we observed notable changes in the morphology of the peroxisomes, characterized by significant increases in both size and number (Fig4G-H). This suggests a cellular adaptation aimed at maintaining lipid metabolic homeostasis, potentially in response to the altered lipid availability or in compensation for proteasome hyperactivation. Such adaptations could enhance the peroxisomes' ability to process lipids (i.e. β-oxidation), thereby compensating for the scarcity or altered composition of LDs.

In *C. elegans*, an important aspect of lipid droplet biology is the interaction with vitellogenins, key lipoproteins that, while not found within these organelles, are associated with them in the process of lipid recruitment during yolk biogenesis[75,76]. In aging *C. elegans*, the dysregulation of vitellogenin expression leads to the abnormal buildup of yolk proteins and lipoproteins[77–80]. This aberrant accumulation is linked to a cascade of adverse effects, including senescent proteinopathy, organ degeneration, obesity, and proteotoxicity[77–80]. These observations highlight the critical role of lipid droplets and their constituent proteins in maintaining cellular homeostasis and underscore their potential impact on age-related diseases and metabolic disorders. *C. elegans* vitellogenin is the homolog of human ApoB[81] which is degraded via ERAD[82], hence we expect that the proteasome likely also catalyzes vitellogenin degradation.

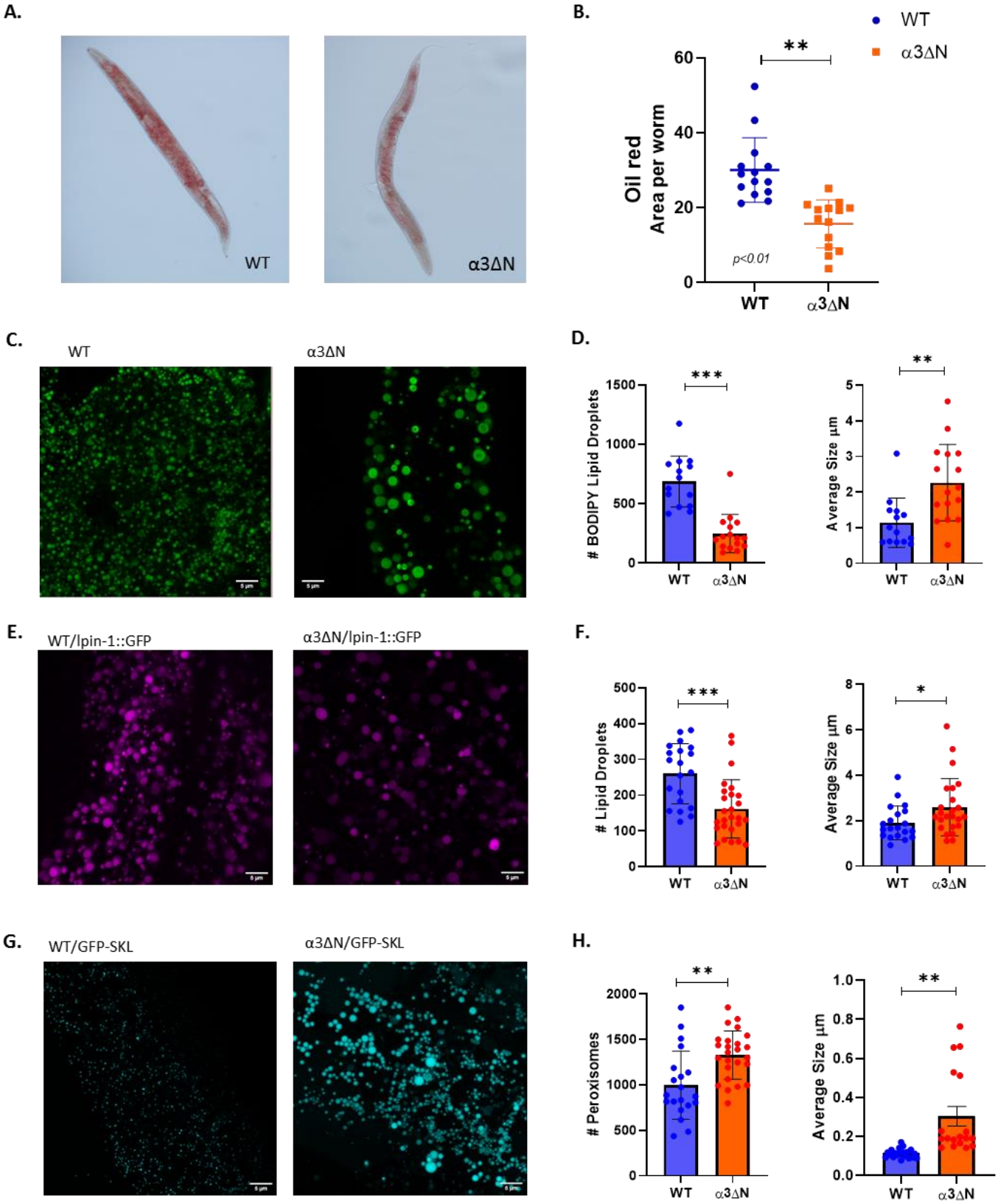

Figure 4. Reshaping Lipid Storage and Peroxisomal Profiles in open gate α3ΔN Mutants. A. Representative images of Oil Red O staining in WT and α3ΔN adult worms at 10x magnification. **B.** Quantification of the area stained by the Oil Red O in in WT and α3ΔN adult worms. n = 14. Error bars represent mean ± SD. $^{**}p<0.01$ by unpaired two-tailed *t*-test. **C.** BODIPY labelled lipid droplets, in WT vs α3ΔN worms. Fluorescence image of the anterior part of living worms (intestine) at 63x magnification. Scale bars, 5 µm. **D.** Number and size of lipid droplets in (n=14) WT and (n=16) α3ΔN worms after staining with BODIPY. **E.** Representative images of endogenous lipid droplets tagged with lpin-1::GFP in WT/lpin-1::GFP and α3ΔN/lpin-1::GFP . . Fluorescence image of the anterior part of living worms (intestine) at 63x magnification Scale bar, 5µm. **F**. Number and sizes of lipid droplets tagged with lpin-1::GFP (n=20) WT, and n=(26) α3ΔN worms. **G.** Representative images of peroxisomes assessed by fluorescence in WT and α3ΔN worms expressing a peroxisome-localized GFP (GFP–SKL) driven by the eft-3 promoter (eft-3p::3XFLAG::GFP–SKL). Images of anterior part. Scale bar, 5 µm. **H.** Number and sizes of peroxisomes in (n=20) WT, and (n=25) α3ΔN worms. **(D,F,H)** Data are the mean ± S.E.M. Each dot represents the number of lipid droplets **(D,F)** or peroxisomes (**H)** in a 59 × 59 µm area in the anterior region (intestine) of individual worms. To determine the size of peroxisomes (n=20) WT and (n=18) α3ΔN worms were imaged at 63x with a 2.5 zoom increase. $^{*}p < 0.05$, $^{**}p < 0.01$, $^{***}p < 0.001$ by unpaired two-tailed *t*-test.

We found that the entire vitellogenin family is downregulated significantly at the protein level according to proteomics (Fig S4B), but no significant changes by fold change were found at the transcript level by RNA-seq (Fig S4C), suggesting a regulation at the protein level by the hyperactivation of the proteasome rather than a transcription interference. To validate this, we specifically monitor vitellogenin levels, by using a *C. elegans* strain expressing a Vitellogenin-GFP fusion protein (VIT-2::GFP) RT99 (Fig5A). After crossing our hyperactive proteasome mutants with the RT99 strain, we quantified GFP levels. The results showed a significant decrease in VIT-2::GFP fluorescence in the open gate worms (50% reduction of VIT-2::GFP consistently across the population) (Fig 5A-B) and this decline remained consistent through the aging process (FigS4D), corroborating the vitellogenin depletion detected in our omics data and suggesting enhanced ERAD in the α3ΔN open gate mutant worms. We confirmed proteasome-dependent degradation of VIT-2 by using MG132 to specifically inhibit proteasome activity. Within three hours of exposure, we observed a significant increase in GFP fluorescence in worms treated with MG132 (Fig5C-D). This increase in fluorescence directly supports the hypothesis that VIT-2 degradation is reliant on proteasomal activity.

Proteasome hyperactivation enhances ERAD function

A conundrum with the above degradation results is that Vit-2 and GFP have well-structured domains, that would preclude them from being degraded by the open-20S proteasome without unfolding. However, the process of ERAD requires unfolding to extract proteins from the ER by P97/VCP, thus fulfilling the requirement for 20S dependent degradation[83]. P97 was also slightly upregulated (0.18 fold change, statistically significant, Table S1) in our TMT-MS dataset. To further investigate the ERAD pathway, we treated our strain with tunicamycin, a compound known to trigger the UPR by disrupting ER glycosylation and protein folding, thereby affecting ERAD[84,85]. Our results showed worms with the open gate mutations demonstrate a significant improvement in survival rates, supporting a conclusion for the enhancement in ERAD efficiency (Fig5E). Generally, ER stress would lead to an increased sensitivity to tunicamycin; however, this was not observed in the α3ΔN strain, implying a different mechanism at play in upregulating the UPR response we observed. This finding highlights the beneficial impact of enhanced ERAD pathways in the α3ΔN mutants, potentially offering insights into mechanisms that help mitigate aging-related declines in protein quality control and overall organismal health.

We further explored the ERAD enhancement's disease implications with an orthogonal approach by crossing the α3ΔN into a *C. elegans* model for Alpha-1 antitrypsin deficiency (A1ATD), a condition marked by accumulation of ATZ in the ER[86]. ATZ represents another angle of proteostasis dysfunction. Due to a genetic mutation, these misfolded proteins accumulate in the liver, hindering its function and elevating the risk of liver diseases[38,87]. ATZ is directly associated with the ERAD pathway, making it heavily reliant on proteasome activity for the clearance of misfolded alpha-1 antitrypsin proteins. Remarkably, α3ΔN mutants showed significantly reduced accumulation of sGFP-ATZ (Fig5F-G, FigS4E), and this reduction persisted with aging (FigS4F), indicating improved management of aberrant proteins. This suggests the α3ΔN mutant's potential for therapeutic strategies targeting ATZ, where proteostasis is disrupted.

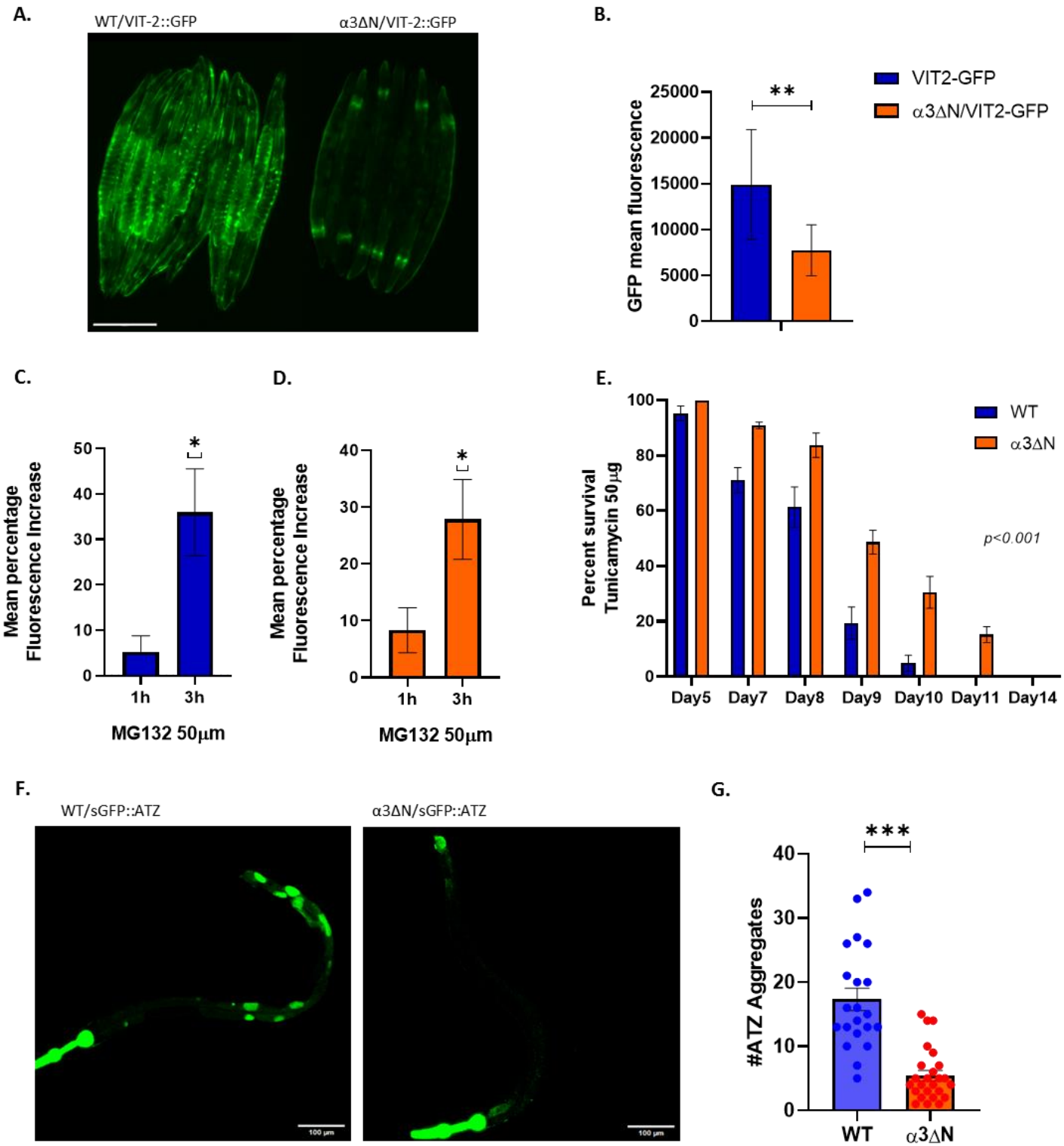

Figure 5. Enhanced ERAD in α3ΔN Mutants Reduces Vitellogenin and Pathogenic ATZ Accumulation. Representative images **(A**) and fluorescent quantification (**B**) of WT/VIT-2::GFP and α3ΔN/VIT2-2::GFP worms expressing the vitellogenin 2 protein fused to GFP vit-2::GFP strain RT99 with defective accumulation of vit-2. Scale bar 500µM. Images of the worms at 4x. Data in **B** represents mean values ± SD $^{**}p < 0.01$ by two-tailed *t*-test. **C-D.** VIT-2::GFP validation as proteasome substrate by quantifying GFP fluorescence after addition of proteasome inhibitor MG132 (50µM) to the WT/VIT-2::GFP (C) and α3ΔN/VIT2-2::GFP (D) adult worms. Data represents mean values ± SD (n=6) $^{*}p < 0.05$ by two-tailed *t*-test with welch correction. **E.** Survival of WT animals and **α**3ΔN Mutants upon tunicamycin treatment 50 (µg/mL) (data from $n = 3$ independent experiments) $p<0.01$ determined by the log-rank test. **F.** Representative Imaging of transgenic animals expressing ERAD substrate (s)GFP::ATZ in intestinal epithelium. Scale bar, 100 µm. **G.** ATZ Aggregate Quantification: Comparison of ATZ aggregate counts in WT/sGFP::ATZ (n=21) and α3ΔN/sGFP::ATZ (n=25) worms on day 5. Data represents mean values ± SEM $^{***}p < 0.001$ by two-tailed unpaired *t*-test.

Alternative splicing changes in open gate mutants

Given the alterations in mRNA processing highlighted by omics data enrichment in our study, and considering the observed increases in translation rates in our α3ΔN mutants, we hypothesized potential impacts on alternative splicing (AS). Utilizing rMATS (replicate Multivariate Analysis of Transcript Splicing)[88] we quantified the amount of AS on the α3ΔN mutants. Our findings revealed minimal alterations in AS events (Fig6A- FigS5A-D). Despite the splicing events being statistically significant, a closer examination of the sashimi plots revealed minimal visual distinctions in some cases, suggesting that while these AS events are indeed statistically significant, their biological impact or the magnitude of splicing change was not always visually pronounced. We found that specifically, Skipped Exons (SE) and Alternative 3´ Splice Site (A3SS), which have the capacity to indirectly influence polyA site choice through modifications in the mRNA transcript that affect the sequence or structural context around the polyA signal were the type of AS with the most occurrences in the α3ΔN mutants. This indirect influence in polyA site selection is critical, as it can affect mRNA stability, nuclear export, and translational efficiency, the latter being significantly increased in α3ΔN mutants. However, we found no changes in alternative polyadenylation usage (FigS5E) when we quantified alternative polyadenylation by using DaPars 2.0[89]. This set of results aligns with the known RNA processing patterns in *C. elegans,* which typically exhibit low variation in exon usage and confirms that mRNA processing changes in open gate mutants likely impact ribosomal regulation and translational rates rather than creating a diverse isoform profile[90,91].

However, an interesting exception was observed among the differential AS, specifically in the spastin gene, exhibiting a significant alternative splicing event: the increased inclusion of exon 4 in α3ΔN open gate worms by 20% (Fig 6B-C). SPAS-1 is notable for having two isoforms in *C.elegans*, which arise through alternative splicing on exon 4 generating SPAS-1L and SPAS-1S[92]. The exon 4's amino acid sequence aligns with motifs from known functional domains from human and *Drosophila* that compose the microtubule binding domain (MTBD). This AS indicates that the function of spastin-1L in α3ΔN might be altered[93]. It has been discovered in humans that there are three variants of spastin mRNA, specifically in exons 4, 8, and 15, though the distinct functional roles of these variants remain unclear[93,94]. To understand potential structural differences caused by exon 4, we used AlphaFold Multimer[95] and generated both hexameric structures, without exon 4 and with exon 4 inclusion (Fig6D Exon 4 in orange). According to the structures, the domain from exon 4 is near the substrate entry/binding surface, where mutations impact its function[93]. The connection between the splicing variation and its functional outcomes warrants further investigation. However, it is plausible that this variation contributes to the observed lipid droplet (LD) phenotype and the increase in peroxisomes. This hypothesis is supported by spastin's known functions in lipid droplet binding, biogenesis, and the promotion of fatty acid transfer to mitochondria and peroxisomes[96,97]. In addition, this inclusion could be related to improving the severing/disassembly of microtubules functions, which are diminished in neurodegeneration, hence, tightly related to proteome health in ageing.

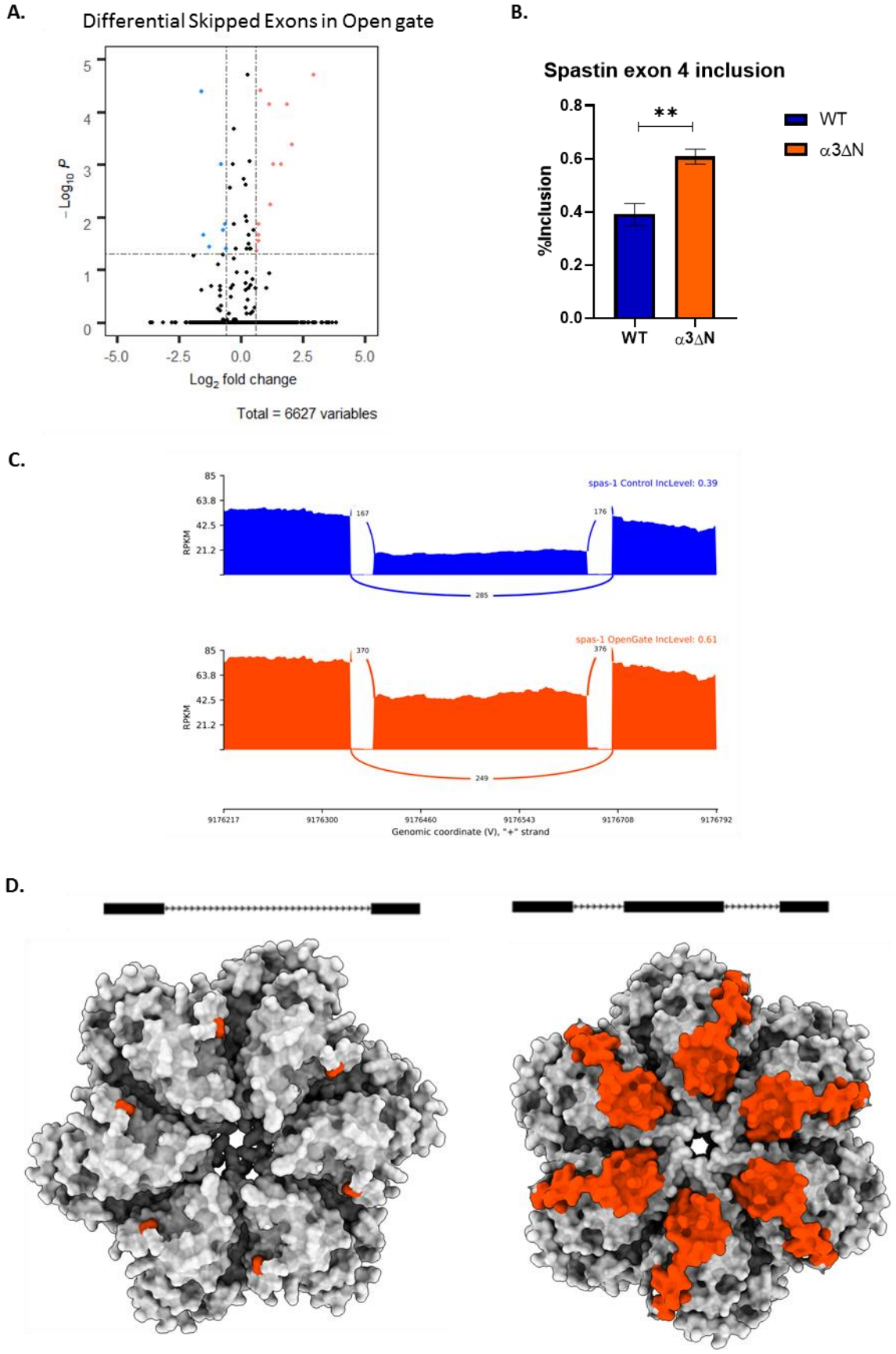

Figure 6. Open gate α3ΔN mutant impacts alternative splicing of spastin (spas-1) in *C. elegans.* A. Alternative splicing analysis on α3ΔN mutants. Volcano plot depicting differential Skipped Exons changes in the percentage of spliced exon inclusion (ΔInc) in α3ΔN vs WT worms. Blue points above the x axis dotted line represent excluded exon events (ΔInc-10%) and orange dots represent included exon events (ΔInc>10%). Significance was determined with RMATS *(FDR<0.05)* **B.** Percentage of inclusion in α3ΔN mutants for spastin exon 4 compared to WT. **C.** Sashimi plots illustrate spastin exon 4 inclusion differences, with WT shown in yellow and α3ΔN mutants in red. **D.** Alphafold-multimer homooligomeric reconstruction models of spastin without exon 4 (left) and with exon 4 inclusion (right), highlighting the spliced region in orange.

A Unique Genetic Profile

The comparative proteomic analysis presented in supplemental figure 6 unveils the unique genetic profile and regulatory networks associated with the open gate α3ΔN mutant's response. By comparing the protein expression profiles of α3ΔN with those of mutants exhibiting similar phenotypes, such as lifespan extension (daf-2 mutants and dnj-21 mutants), lipid reduction (eat-2 mutants) and heat shock network regulation (starvation mutants), we aimed to identify the distinctive features of the α3ΔN mutant's response[11,98–100]. The Circos plot (Fig S6A) and comparative analysis (Fig S6B) revealed a low degree of similarity in impacted genes and regulatory pathways between the α3ΔN mutants and other mutants, despite some phenotypic parallels. Metascape[101] analysis (Fig S6B) identified the most significant shared biological processes and pathways among the mutants, including fatty acid metabolism, regulation of longevity, DNA replication and ribosome biogenesis. The network of interactions (Fig S6C) visualizes the similarities in proteins modulated color-coded according to the scheme used in the Circos plot and showed limited examples such as minichromosome maintenance protein complex (MCM) involved in DNA replication, ribosome subunits, fatty acid elongases elo and SOD-3. The relatively small portion of proteins colored for α3ΔN mutant node (red) suggests a limited overlap in protein expression with other mutants, reinforcing its distinct response. Interestingly, the α3ΔN mutant did not show significant differences in the expression of master regulatory genes linked to *C. elegans* longevity and stress response, such as dnj-21, hsf-1, daf-16, and eat-2 (Fig S6D). This finding indicates that the α3ΔN mutant's unique response is not driven by the differential expression of these well-known regulators but rather stems from the hyperactivation of the proteasome. In conclusion, the multi-omics analysis demonstrates that the open gate α3ΔN mutant exhibits a distinctive genetic profile and regulatory network, setting it apart from other mutants with similar phenotypes. The network of interactions highlights the limited overlap in gene expression between the α3ΔN mutant and other mutants, underscoring the significance of proteasome hyperactivation in its unique phenotype.

Discussion:

Aging-related proteinopathies and neurodegenerative conditions severely compromise the health of older individuals, posing substantial challenges to public healthcare systems[1,10]. The accumulation of misfolded and aggregated proteins, particularly intrinsically disordered proteins (IDPs), is a hallmark of these disorders, implicating the role of the proteostasis network and the proteasome system in maintaining cellular health[15–17]. Our study highlights the potential of targeting the 20S proteasome, a crucial regulator of IDP degradation, as a promising therapeutic strategy for these conditions. Previous studies in yeast genetic models with mutant α-3 subunits have shown that yeast can tolerate the mutation, but are slow to exit G0 of the cell cycle[102]. Cell line studies in mammalian systems overexpressing a truncated α-3 subunit have demonstrated resistance to tau overexpression[103]. Additionally, several proteasome overexpression studies, via α subunit overexpression, have shown increased degradation rates, resistance to oxidative stress, and altered ubiquitination patterns [24–27,103]. However, this study differs from those as it comprehensively analyzes the proteomic impact of proteasome catalytic hyperactivation (not protein increase) in a multicellular organism. Combined, these findings provide further support for the potential therapeutic benefits of proteasome hyperactivation in the context of neurodegenerative diseases and age-related proteinopathies.

Using a *C. elegans* model with a constitutively open-gate 20S proteasome (α3ΔN), we demonstrated that proteasome hyperactivation leads to extensive cellular rewiring, as evidenced by significant changes in the proteome and transcriptome (Fig.1, Fig.2). The simultaneous increase in protein synthesis and degradation rates (Fig.1D-E) suggests a dynamic response to proteasome hyperactivation, aimed at maintaining proteostasis. Differential expression analysis revealed alterations in genes and proteins involved in proteostasis, including those linked to oxidative stress defense (Fig.2F-G), highlighting the adaptive mechanisms employed by the cell to cope with enhanced proteasomal activity. Interestingly, a decrease in cytosol SOD-1 which is a known aggregate prone protein[5], and sHSPs were observed, likely due to increased degradation of misfolded or oxidatively damaged proteins (Fig. 3A), which reduced the demand for these proteostasis factors.

Proteasome hyperactivation reduces the presence of IDPs (Fig.1F), which is particularly relevant to neurodegenerative diseases, as many pathological proteins that misfold and accumulate in these disorders, such as amyloid-beta (Aβ), tau, α-synuclein, and Huntington, are also IDPs [3,6,52,104–107]. Our omics data demonstrated an upregulation of RNA and DNA-binding proteins in α3ΔN mutants, suggesting accelerated degradation of these. Recently, Pepelnjak, M. *et al* identified 20S substrates as primarily RNA- and DNA-binding proteins with intrinsically disordered regions[44].The increased levels of these genes or proteins would be expected if their degradation rates were very high, requiring high levels of synthesis to provide the needed cellular demand for the essential biological functions of RNA and DNA-binding proteins.

One of the key findings of our study is the enhanced resistance to oxidative stress (H2O2, tBOH, and Juglone) observed in α3ΔN mutants (Fig.3) and the identification of the likely underlying mechanisms. Several mechanisms may play a role in this increased resistance: 1) generally enhanced protein degradation, 2) enhanced UPR activation and 3) peroxisome proliferation (the latter 2 discussed more below). The decreased oxidation levels in specific peptides (Fig.3A) support the notion of enhanced degradation of oxidatively damaged proteins, however, reduced oxidative environment due to mediation from peroxisome proliferation could also play a role. Importantly, the sustained resistance to oxidative stress in aged worms (Fig. 3E) underscores the durability of this proteasomal protective mechanism, which has significant implications for age-related diseases characterized by increased oxidative damage. Notably, the open-gate 20S strain still protects worms even in the absence of all superoxide dismutases (SODs), demonstrating protection even during oxidative conditions, indicating direct degradation of damaged proteins likely plays a role in protection.

Our multi-omics approach revealed surprising and profound impacts of proteasome hyperactivation on lipid homeostasis, and peroxisome populations (Fig.4). The marked reduction of lipids, alongside alterations in lipid droplet and peroxisome profiles (Fig.4A-H), suggests a complex interplay between proteasome activity, lipid metabolism, and organelle function. The changes in lipid droplet number and size, as well as the increased number and size of peroxisomes, in agreement with omics data, point to a remodeling of lipid storage and processing mechanisms in response to enhanced proteasomal activity. Though the mechanism by which 20S gate opening effects LD biology is not understood, we speculate it could be related to the proteome enhancement in ERAD function and capacity. Following this, our analysis of alternative splicing revealed a significant event in the spastin gene (Fig.6A-C), with increased inclusion of exon 4 encoding part of the microtubule-binding

domain. The potential functional consequences of this splicing change could be related to the observed changes in lipid droplet and peroxisome dynamics, given spastin's known roles in organelle trafficking and lipid metabolism. Further investigation of this splicing event may provide insights into the link between proteasome activity, cytoskeletal regulation, and organelle homeostasis.

Several proteins implicated in TAG synthesis and fatty acid regulation were identified as downregulated, contributing to a lipid reduction phenotype commonly observed in long-lived mutants[108,109]. The upregulation of enzymes involved in peroxisomal fatty acid β-oxidation (acs-3 and acdh-8) further supports a compensatory mechanism to maintain energy homeostasis in the face of altered lipid metabolism and could even be the case of reduced LDs in α3ΔN. Peroxisome dysfunction has been implicated in various age-related disorders, including neurodegenerative diseases, cancer, and metabolic syndrome. For example, peroxisome biogenesis disorders (PBDs) are a group of genetic diseases characterized by impaired peroxisome function, leading to severe neurological and developmental deficits[73,110]. Thus peroxisomes play crucial roles in various cellular processes, and their proliferation in the α3ΔN mutant may have significant implications for health and longevity. They are essential for the β-oxidation of very long-chain fatty acids (VLCFAs) and the biosynthesis of ether-phospholipids, which are important components of cellular membranes, particularly in the nervous system[73,110,111]. The increased number and size of peroxisomes in the α3ΔN mutant could enhance these processes, potentially improving membrane integrity and neuronal function, which are often compromised in age-related diseases. Furthermore, peroxisomes house enzymes like catalase and peroxiredoxins that decompose hydrogen peroxide (H_2O_2) and other ROS[112]. Increased peroxisome numbers can enhance the cell's antioxidant capacity and protect against oxidative stress, contributing to the observed resistance to oxidative stress. These findings provide novel insights into the role of the proteasome in regulating cellular metabolism and organelle homeostasis, which may have important implications for age-related metabolic disorders, and neurodegenerative diseases.

Another significant discovery of our study is the improved ERAD efficiency in α3ΔN mutants (Fig.5). The reduced accumulation of vitellogenin and pathogenic ERAD substrate ATZ (Fig.5A-G) indicates a novel role for proteasome hyperactivation in mitigating diseases associated with ERAD dysfunction. Given ATZ's severe impact on liver and lung health due to protein accumulation, our findings on α3ΔN mutants reducing ATZ accumulation are particularly relevant. This suggests a novel therapeutic approach, enhancing proteasome activity could significantly improve protein clearance in ATZ, potentially mitigating liver damage and enhancing lung protection. This approach could benefit ATZ treatment strategies, focusing on the underlying proteostasis imbalance, and offering hope for more effective management of this genetic disorder. Moreover, the enhanced ERAD efficiency has implications for neurodegenerative disorders like Alzheimer's and Parkinson's, which are associated with the accumulation of misfolded proteins often degraded by ERAD. The impairment of the ERAD pathway has been implicated in the accumulation of toxic proteins, such as Aβ and tau in Alzheimer's disease and α-synuclein in Parkinson's disease, leading to ER stress and neuronal dysfunction[113,114]. While further study will be required to understand how proteasome gate-opening may enhance ERAD, we hypothesize that ERAD substrates, which are unfolded during extraction, may directly become substrates of hyperactive 20S proteasomes. The α3ΔN mutant could serve as a valuable tool to investigate the mechanisms by which proteasome hyperactivation

enhances ERAD efficiency and to identify potential therapeutic opportunities for ERAD enhancement.

Vitellogenins typically show unregulated expression during post-reproductive stages, causing misfolding and accumulation leading to death in worms[77,115,116]. However, the α3ΔN hyperactive mutants consistently target these substrates throughout the worms' adulthood (FigS4D). Considering the possibility of ERAD impacts on vitellogenins, like its homolog ApoB[81,117], it is plausible that enhanced activity of these pathways in α3ΔN mutants accelerate the degradation of the vitellogenin family. The selective targeting of vitellogenins may partly explain the observed reduction in fecundity in α3ΔN mutants, as these proteins are important for delivering nutrients to eggs, contributing to reproductive challenges. Proteasome inhibition validated VIT-2::GFP as a proteasome substrate (Fig. 5C-D), reinforcing the enhancement of ERAD in α3ΔN. The enhanced survival upon tunicamycin treatment (Fig. 5E) further highlights the beneficial effects of ERAD pathway enhancement in the context of ER stress. These findings suggest that targeting the proteasome may be a viable strategy for alleviating the cellular burden of misfolded proteins in age-related proteinopathies and other disorders linked to ERAD impairment.

The unique genetic and regulatory profile of α3ΔN mutants, as revealed by comparative analysis with other longevity and stress-resistance mutants (Supplemental Figure 6 A-C), emphasizes the distinct mechanism of action of proteostasis protection through proteasome hyperactivation. The lack of significant changes in key longevity genes, such as dnj-21, hsf-1, daf-16, and eat-2, suggests that the beneficial effects of proteasome hyperactivation are not mediated by triggering these previously described longevity pathways. However, future study and new genetic crosses will be required to conclusively demonstrate the overlapping aspects of how these mutants increase *C. elegans* longevity. This finding highlights the potential of proteasome modulation as a novel approach to promoting healthy aging and combating age-related diseases, independent of established longevity mechanisms.

While constitutive proteasome hyperactivation may have potential side effects or trade-offs, such as the loss of fecundity, no other negative phenotypes have been observed in the α3ΔN mutants. Importantly, the worms appear nominal and have normal motor control, indicating no perturbations to neuronal or developmental functions. In addition, WT and α3ΔN both respond similarly to aldicarb, a neurotoxin indicating that neurons in the α3ΔN function normally and are not stressed. The α3ΔN mutant's unique mechanism of action, independent of canonical stress response and longevity pathways, offers a novel approach to reinstating proteostasis and mitigating the detrimental effects of aging. This suggests that the therapeutic potential of targeting the proteasome could be a promising addition to the landscape of aging interventions.

In conclusion, our study provides compelling evidence for the therapeutic potential of proteasome hyperactivation in the context of neurodegenerative diseases and age-related proteinopathies. By harnessing the power of the proteasome to selectively degrade misfolded, aggregation-prone, and intrinsically disordered proteins, it appears that it may be possible to effectively combat the underlying mechanisms that drive these devastating conditions, as the physiological and omics responses in our α3ΔN animals appear primarily beneficial for many different types of disease. More specific studies on different disease models will be required to fully grasp the potential and full utility of proteasome activation in health. The extensive rewiring of cellular pathways observed in

response to enhanced proteasomal activity, including novel insights into oxidative stress resistance, lipid metabolism, organelle dynamics, and ERAD function, underscores the central role of the proteasome in maintaining organismal health, stress resistance, and longevity.

Methods:

C. elegans strains and culture

C. elegans strains were cultured on nematode growth medium (NGM) agar plates at 20°C, with E. coli strain OP50 serving as the food source, following standard protocols[118]. The N2 Bristol strain was used as the wild-type (WT) control. Unless otherwise mentioned, all experiments were conducted on day 1 of adulthood, focusing exclusively on hermaphrodite worms. Detailed information on the strains utilized in this study can be found in Supplementary Table 5.

TMT-MS- Proteomic changes in α3ΔN mutants

Protein extracts from 8-day old adult populations, were processed using a CME/FASP Digest for trypsinization, followed by labeling with TMT10plex Isobaric Tagging for multiplex quantitative analysis. Post-labeling, samples were fractionated via bHPLC and analyzed on an Orbitrap Eclipse mass spectrometer for high-resolution detection. Data were then processed using MaxQuant [41] against the *C. elegans* protein database to identify and proteins. Proteins identified were loaded in a matrix of raw intensities and processed on R. 3.6.3 for log2 ratio conversion by median sweeping method (Normalization). After normalization and filter for extreme low variance in proteins (count = 0) Principal Component Analysis (PCA) was plotted to visualize the expression patterns among the samples. For Differential Expressed Proteins quantification DEqMS package was used[42] since this method consider the specific structure of MS data and fitted best our data compare to others widely used such as Limma[119]. Proteins with fold changes > |1,5| and false discovery rates (FDRs) < 0.05 were defined as Differential Expressed Proteins (DEPs) and captured for functional enrichment analysis. Regarding intrinsically Disorder Proteins (IDPs), RAPID[35] bioinformatic tool for high throughput inputs was used to obtain the IDP content on the *C. elegans* proteome. Regarding detection and quantification of post-translational modifications (PTMs), focusing on oxidation in α3ΔN mutants we employed MaxQuant which facilitated the identification of proteins and their oxidation states by matching mass spectra against the *C. elegans* protein database, utilizing a site-level false discovery rate (FDR<00.1) to ensure accurate PTM identification[41]. Quantitative data extracted from MaxQuant, including modification-specific peptides' intensities and ratios, were then analyzed to assess the extent of oxidation in R under the Limma package[42].

RNA-seq Transcriptomic changes in α3ΔN mutants:

Total RNA was extracted from samples using TRIZOL™ according to the manufacturer's protocol. RNA Purity, concentration, and integrity were assessed using a NanoDrop One spectrophotometer (Thermo Scientific, Wilmington, DE, USA) and an Agilent Bioanalyzer 2100 system (Agilent Technologies, Santa Clara, CA, USA). All samples had a 260:280 nm ratio between 1.9 and 2.1 and RNA integrity number ≥ 9.5. Samples were sent to Novogene Corporation Inc. (Sacramento, CA, USA) for sequencing in Illumina platform. Data quality control was performed with FastQC v.0.11. After data filtering for adapters, clean reads were mapped to the *C. elegans* WS245 reference genome using HISAT 2.1.0[120]. Then, featureCounts v1.22.2[121] was used to count the number of reads for each of the identified genes. Gene count matrix was filtered for genes with constant values (either 0 or empty). The gene counts were then loaded in RStudio for differential expression analysis

with DESEQ2.0[53]. Counts were normalized using the negative binomial distribution under DESEQ2.0 and genes with log2 fold changes |> 1|, and false discovery rates FDRs < 0.05 were defined as Differential Expressed Genes (DEGs) and captured for further analysis. Principal components analysis (PCA), 3D PCA volcano plots and heatmaps were performed with R v3.6.1 packages in custom in house scripts.

Alternative Splicing (AS) analyses.

For alternative polyadenylation (APA), 3´UTRs were extracted from BAM files and converted in bedgraphs files for Dynamics analysis of Alternative PolyAdenylation from RNA-seq data (DaPars v2.1)[89]. Percent Dynamic Usage of Index (PDUI) was plotted as indicative of changes in polyA site usage (Fig S5A). To detect differential AS events, we used Multivariate Analysis of Transcript Splicing (MATS) turbo package (v) optimized for novel splicing site detection[88]. Exon-centric events from major mRNA processing classes were extracted using WS245 genome GTF files. We identified five key AS events in the aligned BAM files, including Skipped Exon (SE), Alternative 5′ (A5SS) and 3′ (A3SS) Splice Sites, Mutually Exclusive Exons (MXE), and Retained Intron (RI), and integrated these with the reference GTF file. The Inclusion Level Difference (ΔIncLevel) for each exonic event was computed across five biological replicates. AS events were visualized using IGV (version 2.13.2) through Sashimi plots, and downstream data analysis was conducted using R custom scripts.

Enrichment Analysis

Gene Set Enrichment Analysis (GSEA)[43] was performed using the ClusterProfiler[122] library in-house implementation in R studio to assess enrichment signatures in the expression profiles in both TMT-MS and RNA-seq. The entire gene lists were pre-ranked based on the mean fold change and significance (FDR) of each gene. The analysis included the gene set lists from the curated Gene Ontology (GO). The significance of enrichment was set by Benjamini-Hochberg < 0.05. Regarding, proteostasis components enriched categories were identified by hypergeometric distribution FDR < 0.05.

Toxicity assays

Toxicity assays were conducted following the guidelines of Qi Jia & Derek Sieburth[60] using stock solutions of juglone (50 mM in DMSO), tBoOH (70%, 7.2 M), and H2O2 (30%, 9.8 M), freshly prepared before each assay. Synchronized adult *C. elegans* (40–100) were placed in 1.5 mL Eppendorf tubes containing M9 buffer and washed three times. Oxidants were then added at final concentrations ranging from 50–300 µM for juglone, and 100–2000 µM for both tBoOH and H2O2, followed by a 4-hour incubation on a rotating mixer. Post-incubation, worms were washed thrice with M9 and transferred to fresh NGM plates seeded with OP50 for a 16-hour recovery period in the dark at 20°C. Survival rates were determined by counting alive versus dead worms. This procedure was repeated across various concentrations in triplicate for a minimum of two separate experiments. Mortality rates were analyzed using probit analysis through the BioRssay[123] package in R, which also estimated the lethal dose 50 (LD50), 95% confidence limits (CL), slope, and chi-square (χ2) values. Probit regression lines of log concentration against percent mortality facilitated the determination of LD50 values for each treatment, as detailed in Supplemental Figure 3B-E.

Toxicity assays Aldicarb

For Aldicarb a 10 mM stock solution of Aldicarb in DMSO was prepared, and day 1 adult worms were placed on NGM plates containing 1 mM Aldicarb[59]. Survival rates were recorded every 15 minutes

over the course of three independent experiments, with the data presented as means ± SEM. Statistical analysis of the assays was conducted using the survminer and survival packages in R (https://github.com/kassambara/survminer/tree/master).

Endoplasmic reticulum stress with tunicamycin

To induce ER stress we followed the guilades of Gusarov et al. 2021[124], *C. elegans* were placed on NGM plates supplemented with 50 µg/ml tunicamycin in 2% DMSO, and compared to control groups on plates with only 2% DMSO. Treatment started on day 1 of adulthood, with worms being transferred to fresh plates every 2-3 days. Survival rates were monitored daily across three independent experiments, with results expressed as means ± SEM. Data analysis was conducted using the survminer and survival packages in R.

Translation Assay, 6-FAM-dC-puromycin incorporation

To assess protein synthesis, we utilized a fluorescent puromycin incorporation method, employing 2 mM 6-FAM-dC-Puromycin (Jena Bioscience), according to Wang et al. 2013[50] with some modifications for *C.elegans*. Day 1 adult worms were collected in M9 buffer, then rinsed and transferred into S-basal medium. An overnight OP50 bacterial culture was concentrated 10-fold in S-basal medium. Worms were subsequently placed into a mixture of 250 µL S-basal medium, 200 µL of the 10-fold concentrated OP50, and 5 µL of 2 mM 6-FAM-Dc-puromycin, also in S-basal. This mixture was incubated for 4 hours on a rotating mixer. Following incubation, worms were washed three times in S-basal, sonicated, and centrifuged for protein extraction. After sonication, two volumes of S-basal buffer were added, and the mixtures were centrifuged using Amicon Ultra Centrifugal Filters (YM-3, Millipore) to eliminate unincorporated 6-FAM-dC-Puromycin. A minimum of 10% of the reaction products were saved as input to quantify the total nascent protein chains using a plate reader. The incorporation rate was normalized against worms treated with 10 mM Cicloheximide (CHX) alongside 6-FAM-dC-Puromycin, to account for basal levels of protein synthesis inhibition.

Degradation Assay

To evaluate the rates of time-dependent protein degradation, we utilized Cycloheximide (CHX). Worms were exposed to CHX (50 mg/ml in ethanol, Sigma-Aldrich) alone or in combination with the proteasome inhibitor MG132. We distributed and incubated groups of 800–1000 worms each at 20°C for time intervals of 0, 1, 3, and 6 hours. Following treatment, we harvested the worms for total protein analysis. The proteins were separated using NuPAGE 4-12% Bis-Tris gels (Invitrogen) and subjected to electrophoresis. Post-electrophoresis, gels were stained with Coomassie blue dye and then destained over a 24-hour period following standard protocols. To quantify degradation rates, we calculated the treated-to-untreated (CHX/CHX+MG132) protein ratio for each time point. This ratio was then normalized by division with the ratio at the initial time point (0 hours). Protein band intensities were quantified employing the Fiji Band/Peak Quantification Tool (NIH Image).

Analysis of Heat inducible Dirsorder proteins

Synchronized day 1 adult worm populations were collected in M9 Buffer and then diluted with 2× LDS Sample Buffer (Invitrogen). The samples were subjected to a controlled heat treatment to induce disorder in protein conformations, starting with an incubation in a 70°C water bath for 15

minutes, with vortexing every 5 minutes, followed by an increase to 90°C for 5 minutes. This thermal stress disrupts the normal folding patterns of proteins, leading to an increased presence of intrinsically disordered proteins. After the heat treatment, the samples were centrifuged at 6,000 rpm for 15 minutes to remove any insoluble precipitates. The samples were then loaded onto a NuPAGE 4-12% Bis-Tris gel (Invitrogen) for electrophoresis. Following electrophoresis, the gels were stained with Coomassie blue dye and destained over 24 hours according to standard protocols. Protein bands were quantified using the Fiji Band/Peak QuantificationTool (NIH Image).

Oil red O staining for lipid content

To evaluate lipid content, synchronized *C. elegans* were initially washed twice with M9 buffer, then fixed in 2x MRWB buffer (containing 160 mM KCl, 40 mM NaCl, 14 mM EGTA, 1 mM spermidine-HCl, 0.4 mM spermine, 30 mM PIPES at pH 7.4, and 0.2% ß-mercaptoethanol) with 2% paraformaldehyde at room temperature for one hour[125]. Following fixation, worms were rinsed with M9 buffer and dehydrated in 60% isopropanol for 15 minutes at room temperature. Subsequently, they were stained with a 60% Oil Red O solution for 6 hours at room temperature. The stained worms were then mounted on 2% agarose pads and imaged at 10x magnification using a Zeiss Stemi 508 stereoscope and EVOS FV. The intensity of Oil Red O staining was quantified using Fiji software (NIH), according to the specified protocol[125].

Vital staining of LDs with BODIPY 493/503

The BODIPY 493/503 stock solution (1 mg/ml) was prepared in DMSO. Adult worms were incubated in M9/BODIPY 493/503 (6.7 µg/ml) solution for 20 min. An incubation of 20 min generates a sufficient BODIPY 493/503 signal and prevented starvation of the worms and staining of LDs[67]. Next, worms were washed three times with M9 and used immediately for imaging in or Zeiss LSM 710 multiphoton confocal microscope imaged at 63x magnification. Quantification of Number and average size of LDs stained with BODIPY 493/503 was performed using Fiji in a 59 × 59 µm area. The experiment was carried out three times independently. All experiments and analyses were performed in a blinded manner. The lipid droplet numbers and intensities were plotted in Prism 8 and statistically significant differences between samples were assessed using the two-tailed unpaired parametric t-test.

Confocal microscopy

LDs quantification

To visualize lipid droplets by confocal microscopy, we used a reporter strain ABR339 which express the lipid droplet protein lpin-1 fused to GFP, which colocalizes with the LDs marked by Nile Red staining (FigS4A), therefore, this strain can be used as a marker of lipid droplets in *C. elegans*. Lpin-1 protein is orthologous to LIPIN1 in mammals and is also commonly used to measure hypodermal and intestinal lipid droplets[68,126]. Worms were imaged at middle age (adult day 5). In total n=20 WT/ABR339 worms and n=26 α3ΔN/ABR339 worms were imaged in three independent experiments. The worms were mounted on a 2% agar pad, anesthetized with 25 mM sodium azide and covered with a glass coverslide for imaging. Worms were visualized using a Zeiss confocal microscope (LSM710, Axio Observer) equipped with a ×63 oil objective (Plan-Apochromat ×63/1.40 oil DIC M27), utilizing a 1 Airy Unit/45 µm pinhole and 0.5 µm optical section thickness via Zen software (3.0, blue). The anterior intestinal region was specifically captured at 0.18 µm intervals for detailed z-stack confocal imaging. Using Fiji (version 2.1.4), lipid droplet quantifications, and dimension analysis were conducted by creating z-stack projections from individual slices and applying a consistent threshold across all images. The "Analyze Particles" function facilitated the

numeration of lipid droplets, along with the assessment of their perimeter, average size, and diameter within a defined 59 × 59 µm area, ensuring a comprehensive and standardized evaluation of lipid droplet characteristics. The lipid droplet numbers and intensities were plotted in Prism 8 and statistically significant differences between samples were assessed using the two-tailed unpaired parametric t-test

Peroxisome quantification

Peroxisomes were visualized by confocal microscopy using worm the worm strain WBM1177 that express the eft-3p::GFP–SKL fluorophore fused to a peroxisome localization sequence (SKL) [68]. Worms were imaged same age as LDs (adult day 5), unless noted otherwise. For each experiment, n= 20 WT/WBM1177 and n=25 α3ΔN/WBM1177 were imaged. Worms were mounted as described earlier for LD quantification. The anterior region was imaged using the settings described for LDs quantification. Images were processed in Fiji version 2.1.4 by generating z-stack projections of five slices, applying the same threshold to all images and analyzing peroxisomes in a 59× 59 µm area. Peroxisomes usually appeared as fluorescent puncta, therefore, to quantify the size n=20 WT and n=18 α3ΔN were imaged at 63x with a digital zoom of 2.5. All experiments and analyses were performed in a blinded manner. Imaging was performed three times independently. Peroxisome number and size was plotted in Prism 8 and statistically significant differences between samples were tested using the two-tailed unpaired parametric t–test.

Stress reporters hsp-4::GFP and hsp-6::GFP

Transcriptional reporter strains hsp-4::GFP and hsp-6p::GFP crossed into α3ΔN were imaged using a EVOS M7000 microscope. Synchronized worms were grown to day 1 of adulthood at 20 °C, manual picked, immobilized with 25 mM Sodium Azide on slides and imaged within 5 min at 4x and 20x. Imaging was performed three times independently in a total of n=29 worms in hsp-4::GFP and n=10 in hsp-6::GFP strain. GFP intensities were determined using Fiji software (NIH) following the protocol mentioned above and plotted in Prism 8. Statistically significant differences between samples were tested using the two-tailed unpaired parametric t–test.

VIT-2::GFP and sGFP::ATZ

Defective mutants for accumulation of vitellogenin-2 VIT2::GFP strain RT99 and the misfolded human protein, ATZ, involved in human α1-antitrypsin deficiency (ATD) strain were crossed into α3ΔNs. Worms were then synchronized and the accumulation of GFP was measured through the adulthood using EVOS M7000 microscope for VIT2::GFP at 4x or Zeiss LSM 710 multiphoton confocal microscope imaged at 10x magnification for the sGFP::ATZ. Worms were mounted as described earlier for LD and peroxisome quantification. A total of 25 worms were quantified for *sGFP::ATZ* aggregates and at least 10 worms assessed per day in the case of VIT-2::GFP**.** Images were processed in Fiji and quantified as described above, plotted in Prism 8. Unpaired t-test was performed to assess the differences between ATZ aggregates and multiple t-tests were conducted to identify significant differences in VIT-2, with applying the Benjamini, Krieger, and Yekutieli correction (FDR<0.01). Each test was performed on each time point without assuming uniform standard deviation across tests.

Proteasome inhibition assay

Dependency of proteasome degradation for VIT-2::GFP was assessed by treatment with MG132 which completely inhibits WT and open-gate α3ΔN proteasomes. Worms were synchronized and

similarly for toxicity assays were collected in S-basal and exposed to 50µm of MG132 for 1h, and 3h. Afterwards, worms were washed twice with S-basal, lysate and spun down for protein extraction. At least 20% of the total protein products were used as input to estimate the amount of VIT-2::GFP signal in a plate reader. Experiments were performed at least three times independently and percentage of increase was obtained by diving the value of 1h and 3h by the starting value or time 0 of treatment. Significance was obtained with Unpaired t test with Welch's correction.

Structural modelling with AlphaFold Multimer

Structural models of spastin, both with and without exon 4, were predicted using AlphaFold Multimer v2.3.2[95], configured for multimeric assembly predictions to simulate the expected homohexamer formation. The computational analysis was executed on a high-performance computing environment. Inputs comprised six chains for each spastin variant, reflecting the oligomeric state. The analysis was conducted using a reduced database preset, with a template search cut-off set to the most recent structures available up to August 1, 2023, to ensure the incorporation of up-to-date structural information. The models were rendered with ChimeraX.

Omic comparison with other mutants

Comparative omic analyses across different mutants were conducted using Metascape[101], a tool designed for the integrated analysis of multiple independent and orthogonal experimental datasets. Differentially expressed genes (DEGs) identified in each mutant were compiled from the sources, and intersections among these DEG lists were illustrated through Circos plots, enabling a visual representation of genomic relationships and variations. Metascape was used to elucidate of shared biological pathways and functional clusters among the mutants by generating comprehensive heatmaps and enrichment networks, where nodes in the networks were depicted as pie charts. These charts highlighted key shared genes among the mutants, with the size of each pie chart sector proportional to the gene count derived from the collective DEG pool. This representation was applied to elucidate common components enriched across the Omic datasets.

Data and Materials Availability

All processed datasets and materials generated and utilized in this study are provided in the published article and its accompanying supplementary information files. The sequencing data have been deposited at the National Center for Biotechnology Information's Gene Expression Omnibus (GEO) and can be accessed via GEO Series accession number GSE259419. Any additional data pertinent to this study are included within the article, supplementary files, or can be obtained from the corresponding author upon reasonable request.

Acknowledgements

Our sincere appreciation extends to the Smith Lab members for their insightful discussions and feedback throughout the manuscript's development. Special thanks to Aimer Gutierrez-Diaz for his valuable assistance in creating the spastin Alphafold oligomer models, made possible through the computational resources and services at the Institute for Cyber-Enabled Research, Michigan State University. We thank Dr. Kevin Courtney for careful and meticulous review of our manuscript. We also acknowledge Dr. Neil Billington and the West Virginia University Microscope Imaging Facility for their support in conducting the confocal and imaging experiments. The imaging facility has benefitted from the support of the WVU Cancer Institute and National Institutes of Health research

grants P20RR016440 and P30RR032138/P30GM103488. Lastly, we are grateful for the funding from NIH grants R01AG064188 and R01GM107129 awarded to D.M.S., which supported this work.

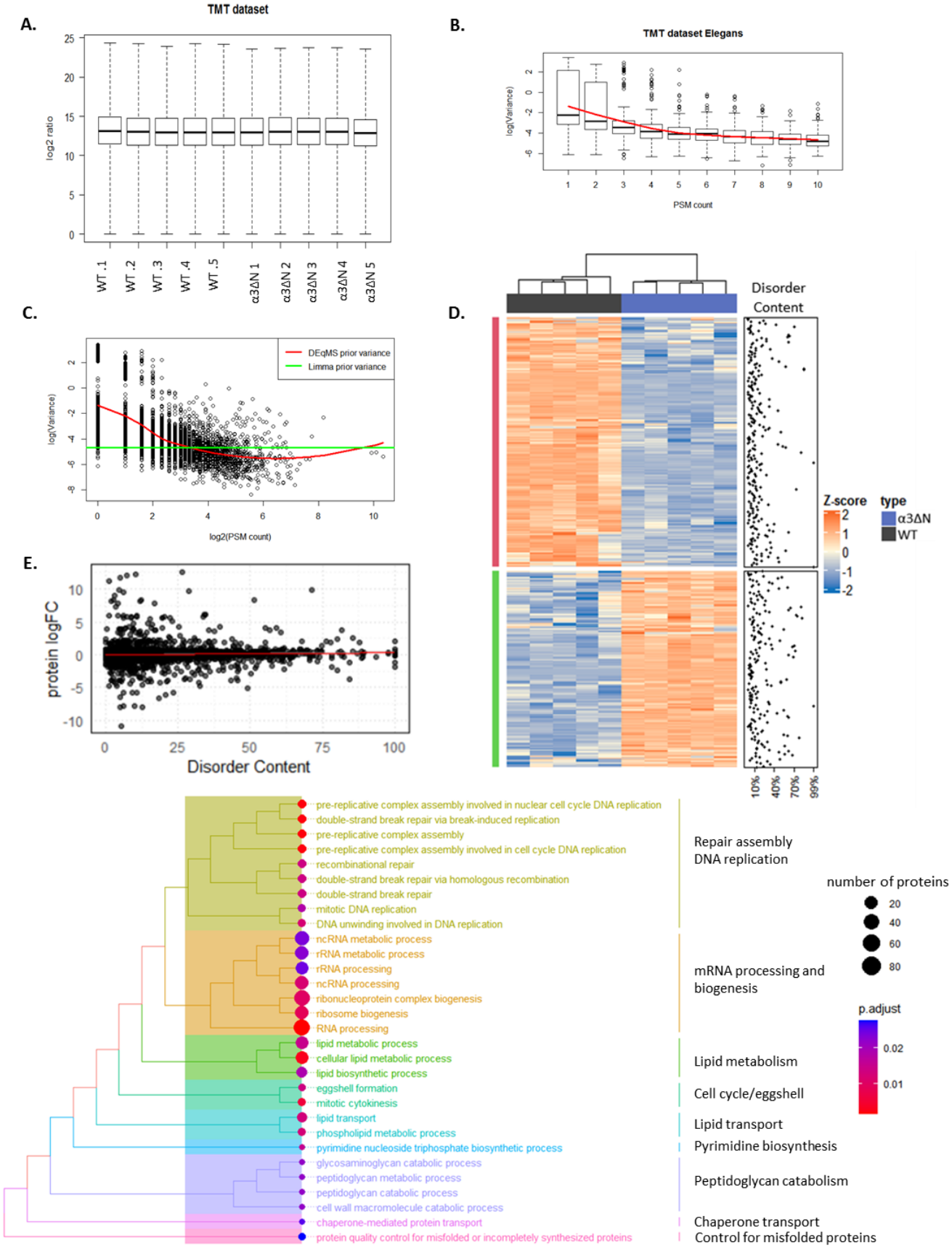

Supplemental Figure 1: Comprehensive Proteomic Analysis and Enrichment in α3ΔN Mutants. A. Boxplot of DEqMS log2 abundance ratios from TMT-MS samples, verifying median-centered distributions. B. The DEqMS fit curve (red line) illustrates variance dependency on peptide spectrum match (PSM) counts, offering insights into sample variability. C. Variance dependency graph showing how variance changes with the number of PSMs, contrasting prior variance estimates by Limma (green curve) and DEqMS (red curve). Individual proteins' pooled variances are depicted as scatter points. D. Heatmap of differentially expressed proteins (DEPs) in α3ΔN mutants, with adjacent scatterplot highlighting the disorder content of these proteins. The hierarchical cluster above the heatmap distinguishes WT (black) from α3ΔN mutants (blue), using z-score values to indicate upregulation (orange) and downregulation (blue) (FDR<0.05 **E.** Scatter plot displays the relationship between protein disorder content (x-axis) and fold change (y-axis) detected by TMT-MS. The marginal histogram above the plot visualizes the density of proteins by expected disorder, color-coded to indicate fold change: yellow). **F.** Treeplot of enriched biological functions from TMT-MS data, clustered by semantic similarity to illustrate the breadth of proteomic alterations in α3ΔN mutants. Seven color-coded clusters summarize key proteomic changes, with each branch ending in a dot representing the category's significance and size, as detailed in the adjacent panel; dot colors correlate with adjusted p-values.for upregulated proteins and blue for downregulated proteins.

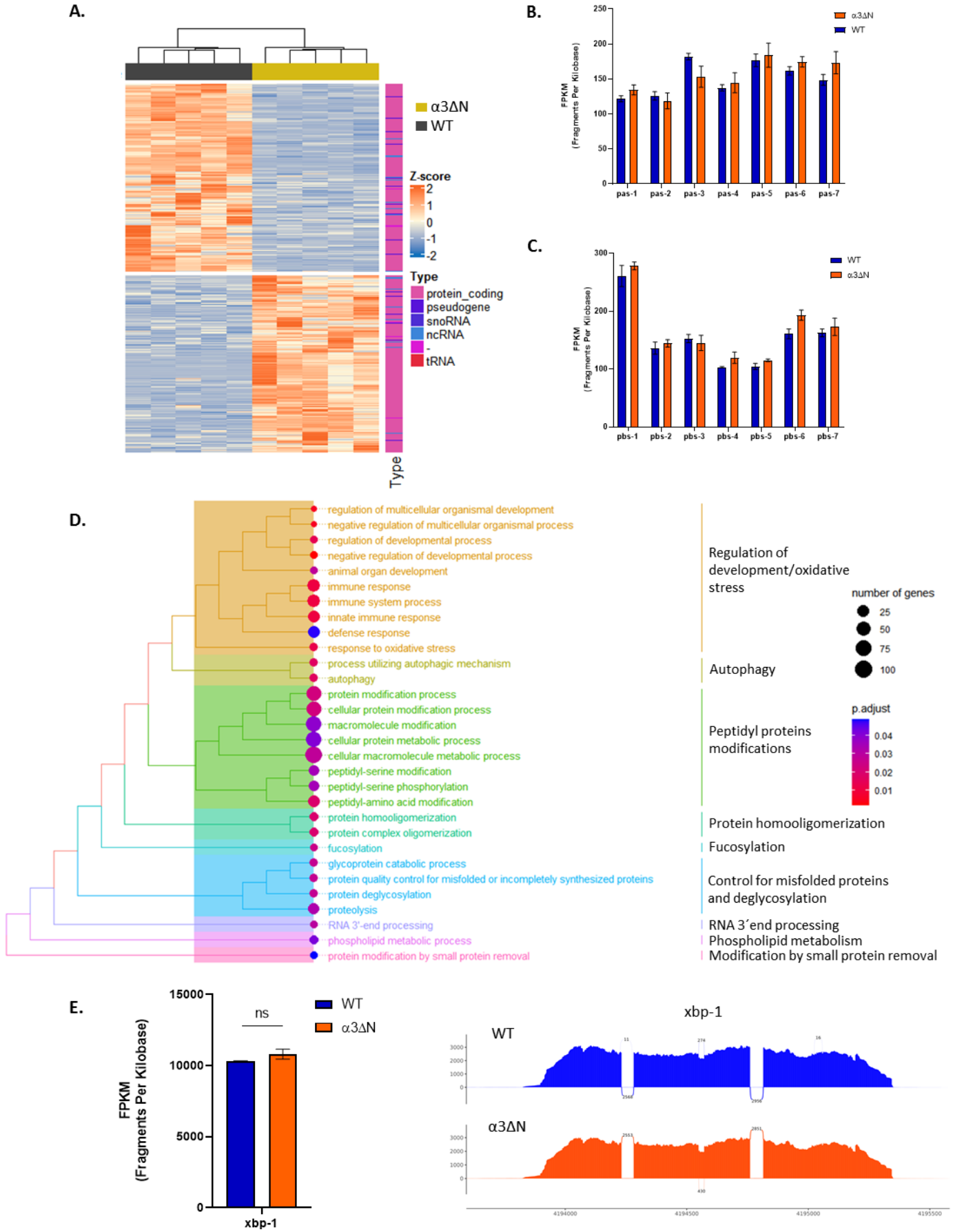

Supplemental Figure 2: Transcriptomic Landscape and Functional Enrichment in α3ΔN Mutants. A. Heatmap visualization shows DEGs in α3ΔN mutants, with a side bar indicating transcript types through color coding, highlighting the predominance of protein-coding genes alongside ncRNAs and snoRNAs. The hierarchical clustering above the heatmap differentiates WT (black) from α3ΔN mutants (yellow), based on z-score values of expression: orange for upregulated and blue for downregulated transcripts (FDR<0.05). **B-C**. Expression Analysis of Proteasome Subunit Genes: Panel B presents FPKM-based expression levels of proteasome α-subunits, and Panel C details the expression of β-subunits in α3ΔN mutants, with data shown as mean ± SEM. No differential expression was observed among these genes. D. Treeplot of Transcriptomic Enrichment. Biological functions derived from RNA-seq data, organized by semantic similarity to reveal comprehensive transcriptomic alterations in α3ΔN mutants. Nine color-coded clusters summarize the principal changes observed, with each branch terminating in a dot that reflects the category's significance and size, as elaborated in the adjacent panel; dot colors correspond to adjusted p-values. **E.** FPKM-based expression levels of xbp-1 and saashimi plot illustrating no changes in xbp-1 isoforms between WT blue and α3ΔN mutants in orange

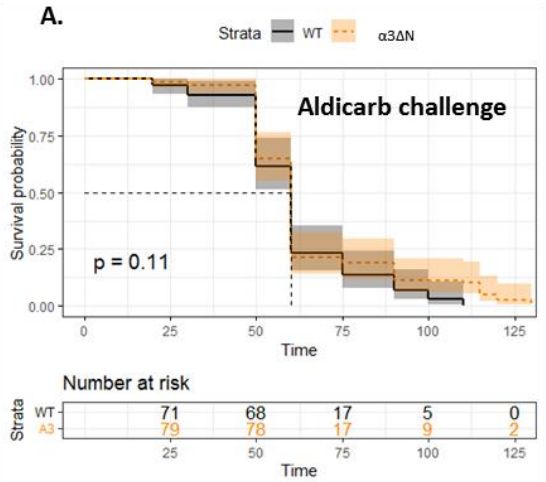

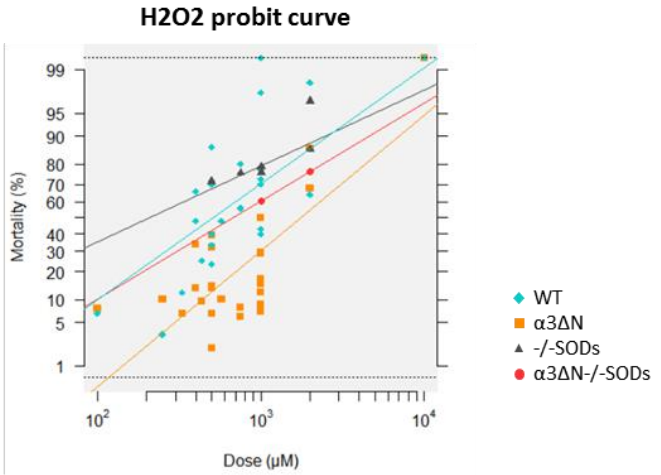

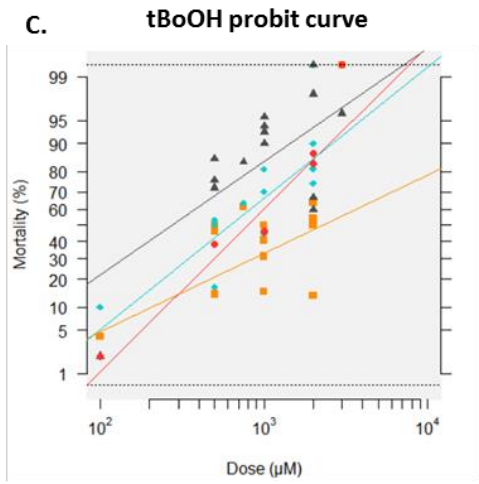

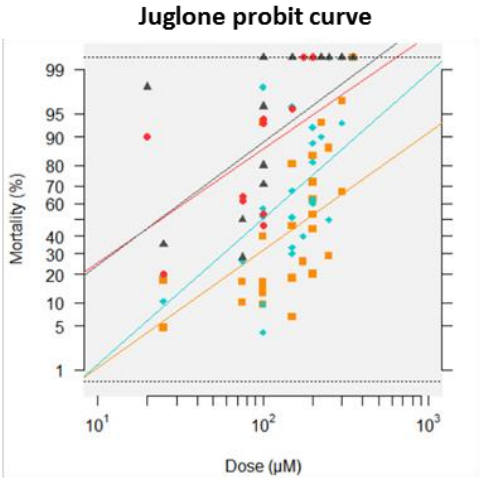

E.

α3ΔN vs WT			
Compound	LD50 μM	RR50	*p-value*
H_2O_2	1758	3.43	0.0025
tBoOH	2260	4.25	0.01667
Juglone	182	1.84	0.0125

	α3ΔN-/-SOD vs -/-SOD				
Compound	LD50 μM	RR50	LD50 μM	RR50	*p-value*
H_2O_2	674	1.32	207	0.4045	0.00179
tBoOH	797	1.28	277	0.4453	0.03492
Juglone	24	0.2429	23	0.236	0.96382

F.

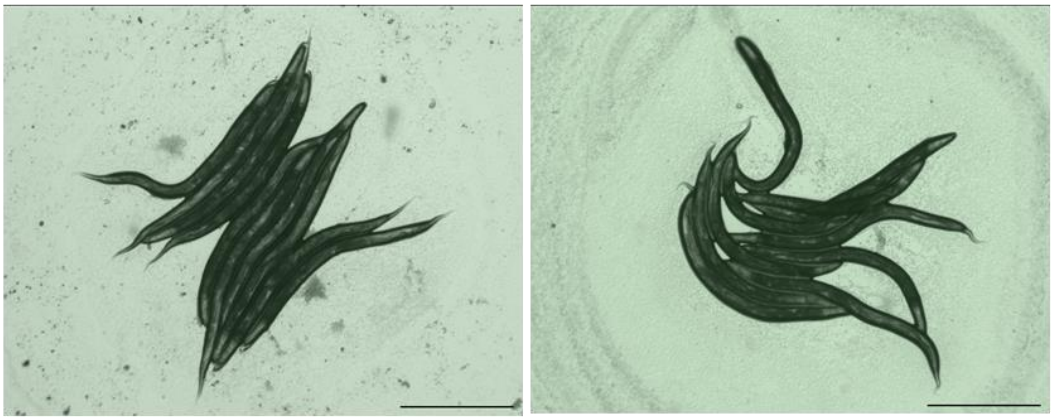

G.

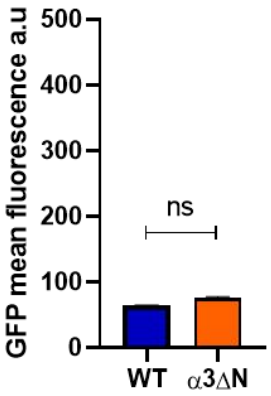

Supplemental Figure 3: Analyzing Oxidative Stress Dose-Response and Mitochondrial Perturbation in α3ΔN Mutants. A. Survival Analysis under Aldicarb Stress. Compares survival rates of WT and α3ΔN mutants exposed to 1mM aldicarb, based on n = 3 independent experiments. Statistical significance assessed via log-rank test (No Significant). B-D. Probit Analysis of Oxidative Stress Dose-Response utilizing the BioRssays package, these plots depict the relationship between probit-transformed mortality rates and log-dose exposure to H2O2, tBoOH, and Juglone. SOD-/- mutants (gray triangles) serve as a susceptible reference; α3ΔN mutants (orange squares) exhibit significantly higher resistance compared to both WT (cyan diamonds) and the SOD-/- reference. Crosses between SOD-/- and α3ΔN (red dots) demonstrate a notable decrease in resistance. E. LD50 Determination and Resistance Ratios for α3ΔN mutants vs WT. Stastical significance was determined by ANOVA with Bonferroni-corrected binomial GLM tests, evaluates strain resistance differences. **F.** Mitochondrial perturbation reporter imaging of WT/hsp-6p::GFP and α3ΔN/hsp-6p::GFP worms under normal conditions. Images captured at 4x magnification. G. Quantification of hsp-6p::GFP Expression: by fluorescence intensity measurement in transgenic worms. Scale bar represents 1250 μm, with data presented as mean ± SEM.

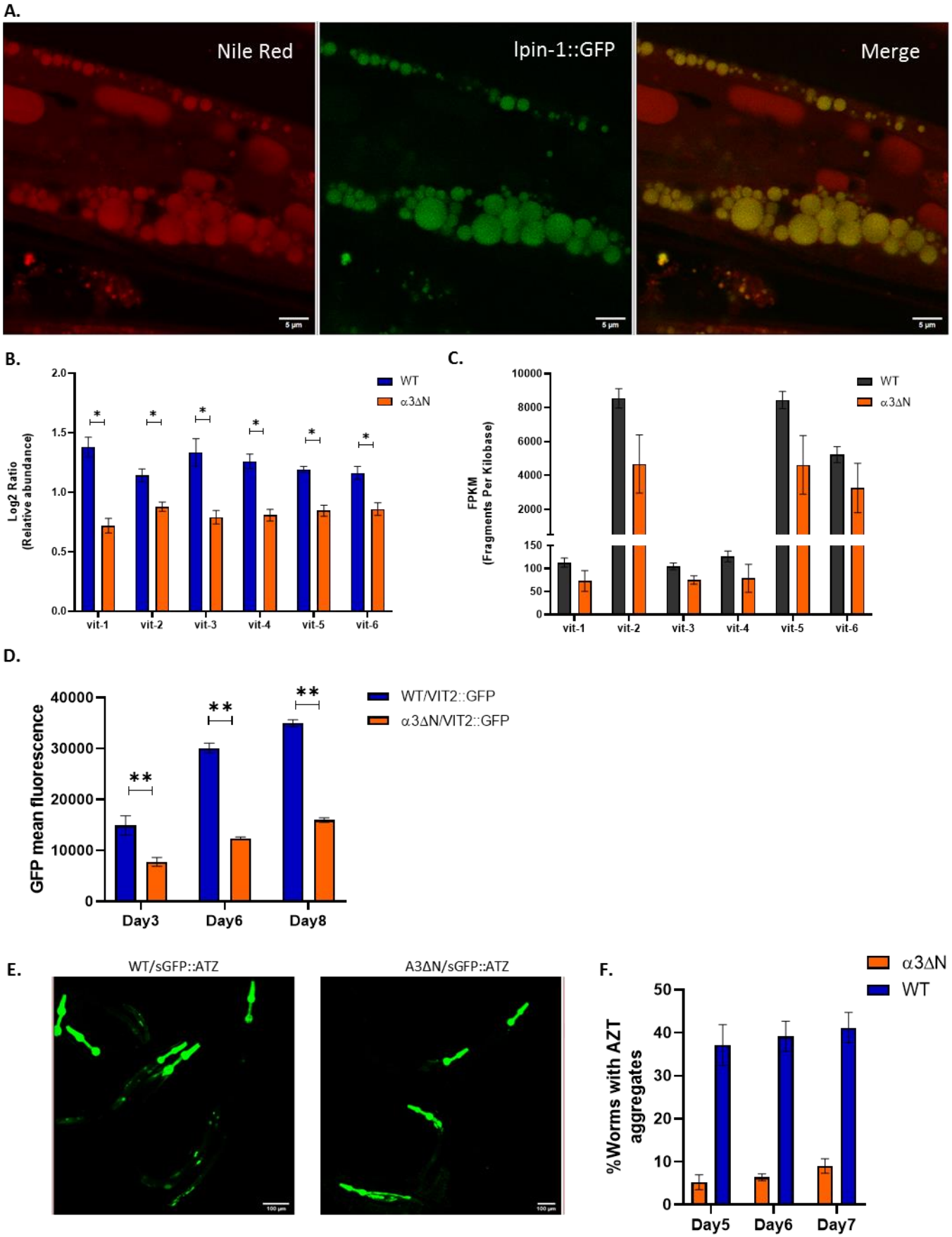

Supplemental Figure 4: Lipid Droplet Reorganization and ERAD Efficiency in α3ΔN Mutants Reflect Proteostatic Adaptation. A. Co-localization in WT worms of Nile Red staining with lpin-1::GFP, confirming GFP-tagged organelles as lipid droplets in *C. elegans*. Z-projections show Nile Red signals (Left), lpin-1::GFP fluorescence (Middle), and their merged visualization (Right). Scale bar 100 µm. **B-C.** Panel B details the log2 relative protein abundance of vitellogenins, indicating altered protein levels in α3ΔN mutants. Panel C presents vitellogenin gene expression measured in FPKM, highlighting transcriptional changes. Both panels feature data as mean ± SEM, with asterisks (*) marking significantly different expressions (FDR < 0.05). **D.** VIT-2::GFP Accumulation Over Time. We tracked the fluorescent intensity of WT/VIT-2::GFP versus α3ΔN/VIT2-2::GFP worms, revealing decrease in VIT-2::GFP accumulation in α3ΔN mutants. Statistical analysis (**p < 0.01) via multiple two-tailed t-tests. Data shown as mean ± SD. **E.** ATZ ERAD Substrate Visualization in Gut Epithelium of transgenic worms expressing GFP-tagged ERAD substrates (sGFP::ATZ) WT/sGFP::ATZ compared to α3ΔN/sGFP::ATZ .Scale bar 100 µm. **F.** ATZ Aggregate accumulation over time in α3ΔN Mutants. Tracking down the formation of ATZ aggregates demonstrates a reduction in sGFP::ATZ aggregates in α3ΔN mutants compared to WT across adulthood, with n=50 for both groups at specified days, showing the enhanced degradation capabilities.

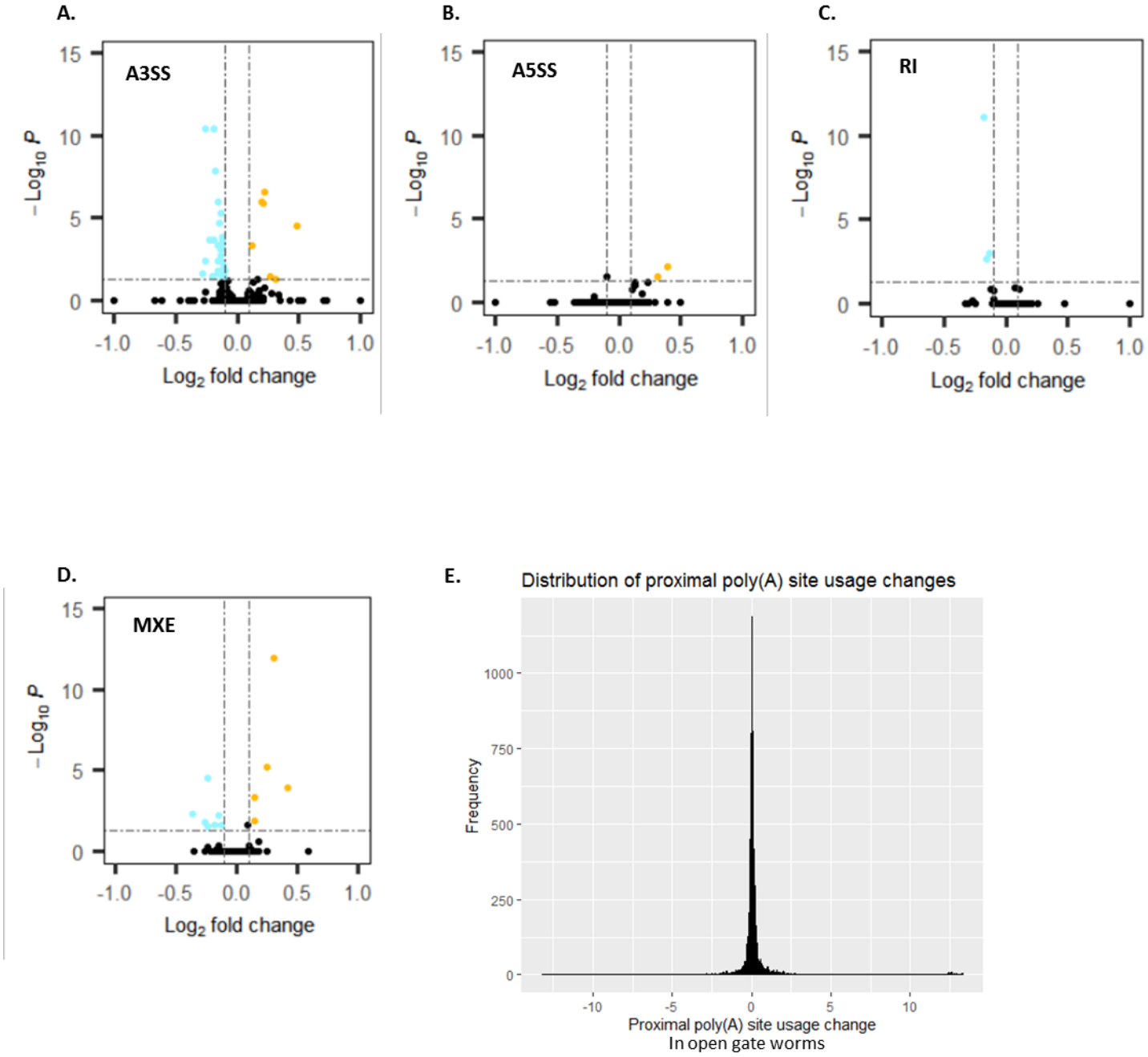

Supplemental Figure 5: Alternative Splicing and Analysis of Polyadenylation Site Selection in α3ΔN Mutants Reveals Stable PolyA Site Usage. **A-D.** Alternative splicing analysis on α3ΔN mutants. Volcano plot depicting differential alternative splicing changes (ΔInc) in α3ΔN vs WT worms. Blue points above the x axis dotted line represent excluded events (ΔInc-10%) and orange dots represent inclusion events (ΔInc>10%). Significance was determined with RMATS *(FDR<0.05)*. **E.** Examination of proximal polyadenylation (polyA) site utilization in α3ΔN mutants via Dapars2.0. Frequency plots illustrate the polyA site usage, predominantly indicating no significant differential usage, with most changes clustered around zero, suggesting stable polyadenylation site selection in open gate mutants.

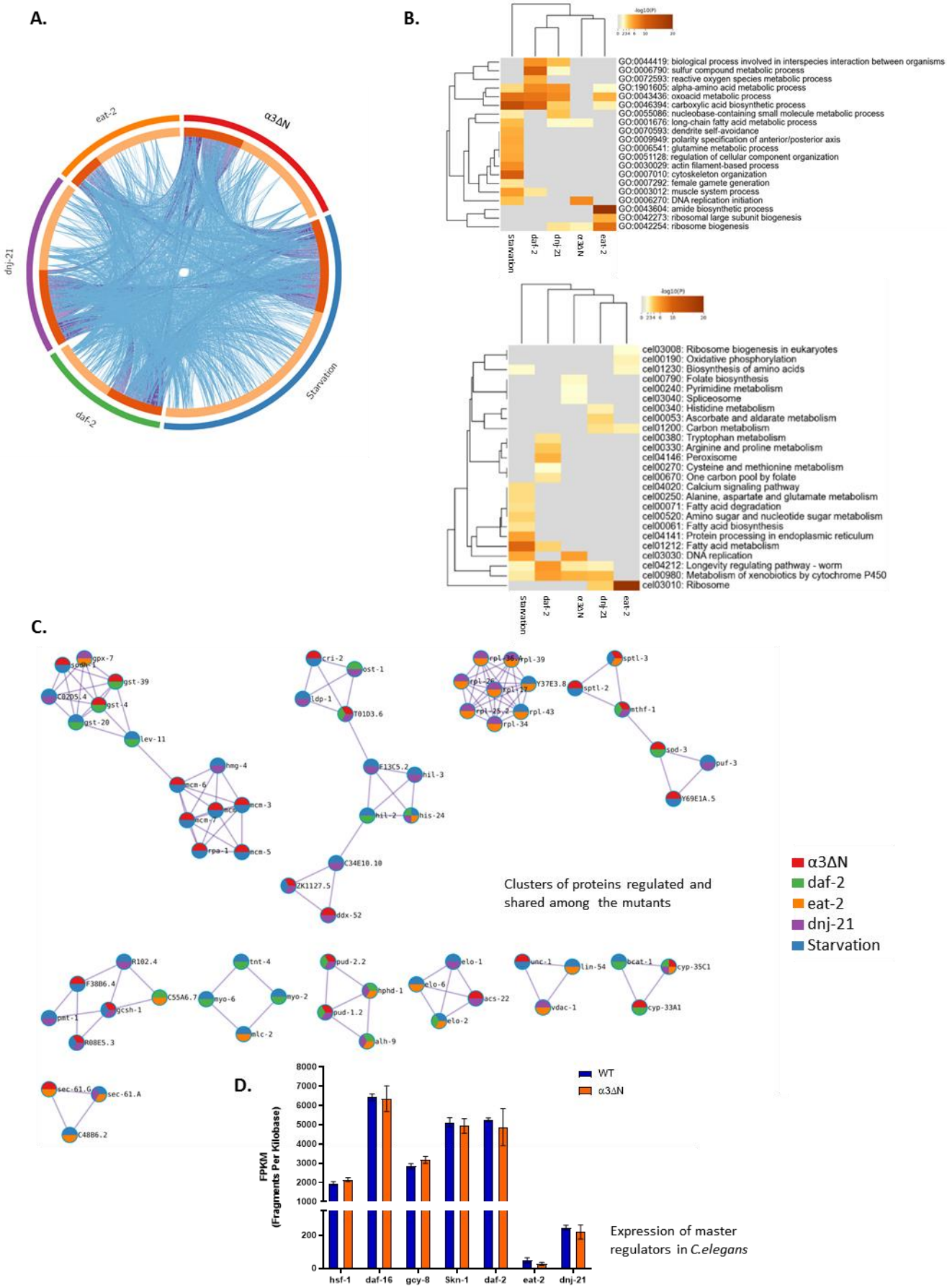

Supplemental Figure 6. Omic comparison with other *C.elegans* long lived mutants reveal a unique genetic profile associated to α3ΔN open gate response. A. Circos plot represented shared changes in expression profiles across several known long live mutant strains. Blue connector lines represent genes shared across the analyzed mutants, whereas purple lines indicate common pathways. The outer ring uses color coding to identify each mutant: red for open gate, blue for starvation, purple for dnj-21, green for daf-2, and orange for eat-2, thus providing a comprehensive overview of shared genetic and pathway features. **B.** Heatmap displays the enrichment of biological processes and KEGG pathways across the mutants, as identified by Metascape analysis. The significance of pathways is visually encoded using a gradient based on -log10(p-value), facilitating an immediate understanding of the most significant pathways across the mutants. **C.** Enrichment networks are depicted as pie charts within nodes, illustrating the distribution of shared genes among the mutants. The color coding for each mutant sector follows the scheme outlined above, offering insights into the complex interplay of genes contributing to longevity and stress defense mechanisms. **D.** The expression of master regulatory genes linked to *C. elegans* longevity and stress response in α3ΔN mutants quantified and visualized in FPKM. Data represents mean ± SEM.

References.

1. Labbadia, J. & Morimoto, R. I. The Biology of Proteostasis in Aging and Disease. *https://doi.org/10.1146/annurev-biochem-060614-033955* **84,** 435–464 (2015).

2. Voges, D., Zwickl, P. & Baumeister, W. The 26S Proteasome: A Molecular Machine Designed for Controlled Proteolysis. *https://doi.org/10.1146/annurev.biochem.68.1.1015* **68,** 1015–1068 (2003).

3. Park, H., Yamanaka, T. & Nukina, N. Proteomic analysis of heat-stable proteins revealed an increased proportion of proteins with compositionally biased regions. *Sci. Reports 2022 121* **12,** 1–13 (2022).

4. Balasubramaniam, D. & Komives, E. A. Hydrogen-exchange mass spectrometry for the study of intrinsic disorder in proteins. *Biochim. Biophys. Acta - Proteins Proteomics* **1834,** 1202–1209 (2013).

5. Ivanova, M. I. *et al.* Aggregation-triggering segments of SOD1 fibril formation support a common pathway for familial and sporadic ALS. *Proc. Natl. Acad. Sci. U. S. A.* **111,** 197–201 (2014).

6. Emin, D. *et al.* Small soluble α-synuclein aggregates are the toxic species in Parkinson's disease. *Nat. Commun. 2022 131* **13,** 1–15 (2022).

7. Cuanalo-Contreras, K. *et al.* Extensive accumulation of misfolded protein aggregates during natural aging and senescence. *Front. Aging Neurosci.* **14,** 1090109 (2023).

8. Hartl, F. U., Bracher, A. & Hayer-Hartl, M. Molecular chaperones in protein folding and proteostasis. *Nat. 2011 4757356* **475,** 324–332 (2011).

9. Balch, W. E., Morimoto, R. I., Dillin, A. & Kelly, J. W. Adapting proteostasis for disease intervention. *Science (80-.).* **319,** 916–919 (2008).

10. Hipp, M. S., Kasturi, P. & Hartl, F. U. The proteostasis network and its decline in ageing. *Nat. Rev. Mol. Cell Biol. 2019 207* **20,** 421–435 (2019).

11. Walther, D. M. *et al.* Widespread Proteome Remodeling and Aggregation in Aging C. elegans. *Cell* **161,** 919–932 (2015).

12. Christianson, J. C., Jarosch, E. & Sommer, T. Mechanisms of substrate processing during ER-associated protein degradation. *Nat. Rev. Mol. Cell Biol. 2023 2411* **24,** 777–796 (2023).

13. Beaudoin-Chabot, C. *et al.* The unfolded protein response reverses the effects of glucose on lifespan in chemically-sterilized C. elegans. *Nat. Commun. 2022 131* **13,** 1–13 (2022).

14. Kumsta, C., Chang, J. T., Schmalz, J. & Hansen, M. Hormetic heat stress and HSF-1 induce autophagy to improve survival and proteostasis in C. elegans. *Nat. Commun. 2017 81* **8,** 1–12 (2017).

15. Vilchez, D., Saez, I. & Dillin, A. The role of protein clearance mechanisms in organismal ageing and age-related diseases. *Nat. Commun.* **5,** (2014).

16. Tai, H. C. & Schuman, E. M. Ubiquitin, the proteasome and protein degradation in neuronal function and dysfunction. *Nat. Rev. Neurosci. 2008 911* **9,** 826–838 (2008).

17. Ciechanover, A. & Kwon, Y. T. Degradation of misfolded proteins in neurodegenerative diseases: therapeutic targets and strategies. *Exp. Mol. Med. 2015 473* **47,** e147–e147 (2015).

18. Upadhya, S. C. & Hegde, A. N. Role of the ubiquitin proteasome system in Alzheimer's disease. *BMC Biochem.* **8,** 1–8 (2007).

19. Ribeiro, F. C. *et al.* Synaptic proteasome is inhibited in Alzheimer's disease models and associates with memory impairment in mice. *Commun. Biol. 2023 61* **6,** 1–12 (2023).

20. Thibaudeau, T. A., Anderson, R. T. & Smith, D. M. A common mechanism of proteasome impairment by neurodegenerative disease-associated oligomers. *Nat. Commun. 2018 91* **9,** 1–14 (2018).

21. Chuah, J. J. Y., Thibaudeau, T. A. & Smith, D. M. Minimal mechanistic component of HbYX-dependent proteasome activation that reverses impairment by neurodegenerative-associated oligomers. *Commun. Biol. 2023 61* **6,** 1–10 (2023).

22. Opoku-Nsiah, K. A. *et al.* The YΦ motif defines the structure-activity relationships of human 20S proteasome activators. *Nat. Commun. 2022 131* **13,** 1–12 (2022).

23. Kors, S., Geijtenbeek, K., Reits, E. & Schipper-Krom, S. Regulation of Proteasome Activity by (Post-)transcriptional Mechanisms. *Front. Mol. Biosci.* **6,** 48 (2019).

24. Nguyen, N. N. *et al.* Proteasome β5 subunit overexpression improves proteostasis during aging and extends lifespan in Drosophila melanogaster. *Sci. Reports 2019 91* **9,** 1–12 (2019).

25. Kapetanou, M., Chondrogianni, N., Petrakis, S., Koliakos, G. & Gonos, E. S. Proteasome activation enhances stemness and lifespan of human mesenchymal stem cells. *Free Radic. Biol. Med.* **103,** 226–235 (2017).

26. Chondrogianni, N., Georgila, K., Kourtis, N., Tavernarakis, N. & Gonos, E. S. 20S proteasome activation promotes life span extension and resistance to proteotoxicity in Caenorhabditis elegans. *FASEB J.* **29,** 611–622 (2015).

27. Howell, L. A., Peterson, A. K. & Tomko, R. J. Proteasome subunit α1 overexpression preferentially drives canonical proteasome biogenesis and enhances stress tolerance in yeast. *Sci. Reports 2019 91* **9,** 1–14 (2019).

28. Anderson, R. T., Bradley, T. A. & Smith, D. M. Hyperactivation of the proteasome in Caenorhabditis elegans protects against proteotoxic stress and extends lifespan. *J. Biol. Chem.* **298,** (2022).

29. Groll, M. & Huber, R. Substrate access and processing by the 20S proteasome core particle. *Int. J. Biochem. Cell Biol.* **35,** 606–616 (2003).

30. Coux, O., Tanaka, K. & Goldberg, A. L. STRUCTURE AND FUNCTIONS OF THE 20S AND 26S PROTEASOMES. *https://doi.org/10.1146/annurev.bi.65.070196.004101* **65,** 801–847 (2003).

31. Babu, M. M., van der Lee, R., de Groot, N. S. & Gsponer, J. Intrinsically disordered proteins: regulation and disease. *Curr. Opin. Struct. Biol.* **21,** 432–440 (2011).

32. Zhao, B., Katuwawala, A., Uversky, V. N. & Kurgan, L. IDPology of the living cell: intrinsic

disorder in the subcellular compartments of the human cell. *Cell. Mol. Life Sci.* **78,** 2371–2385 (2021).

33. Uversky, V. N. Intrinsically disordered proteins and their (disordered) proteomes in neurodegenerative disorders. *Front. Aging Neurosci.* **7,** 132731 (2015).

34. Uversky, V. N. *et al.* Unfoldomics of human diseases: Linking protein intrinsic disorder with diseases. *BMC Genomics* **10,** 1–17 (2009).

35. Yan, J., Mizianty, M. J., Filipow, P. L., Uversky, V. N. & Kurgan, L. RAPID: Fast and accurate sequence-based prediction of intrinsic disorder content on proteomic scale. *Biochim. Biophys. Acta - Proteins Proteomics* **1834,** 1671–1680 (2013).

36. Coskuner-Weber, O., Mirzanli, O. & Uversky, V. N. Intrinsically disordered proteins and proteins with intrinsically disordered regions in neurodegenerative diseases. *Biophys. Rev. 2022 143* **14,** 679–707 (2022).

37. Perlmutter, D. H. α1-antitrypsin Deficiency: A Misfolded Secretory Protein Variant with Unique Effects on the Endoplasmic Reticulum. *Endoplasmic reticulum Stress Dis.* **3,** 63 (2016).

38. Perlmutter, D. H. Pathogenesis of Chronic Liver Injury and Hepatocellular Carcinoma in Alpha-1-Antitrypsin Deficiency. *Pediatr. Res. 2006 602* **60,** 233–238 (2006).

39. Zhang, S., Li, F., Zhou, T., Wang, G. & Li, Z. Caenorhabditis elegans as a Useful Model for Studying Aging Mutations. *Front. Endocrinol. (Lausanne).* **11,** 554994 (2020).

40. Scharf, A., Pohl, F., Egan, B. M., Kocsisova, Z. & Kornfeld, K. Reproductive Aging in Caenorhabditis elegans: From Molecules to Ecology. *Front. Cell Dev. Biol.* **9,** 718522 (2021).

41. Tyanova, S., Temu, T. & Cox, J. The MaxQuant computational platform for mass spectrometry-based shotgun proteomics. *Nat. Protoc. 2016 1112* **11,** 2301–2319 (2016).

42. Zhu, Y. *et al.* DEqMS: A method for accurate variance estimation in differential protein expression analysis. *Mol. Cell. Proteomics* **19,** 1047–1057 (2020).

43. Subramanian, A. *et al.* Gene set enrichment analysis: A knowledge-based approach for interpreting genome-wide expression profiles. *Proc. Natl. Acad. Sci. U. S. A.* **102,** 15545–15550 (2005).

44. Pepelnjak, M. *et al.* Systematic identification of 20S proteasome substrates. *Mol. Syst. Biol.* (2024). doi:10.1038/S44320-024-00015-Y/SUPPL_FILE/44320_2024_15_MOESM10_ESM.PDF

45. Baugh, J. M. & Pilipenko, E. V. 20S Proteasome Differentially Alters Translation of Different mRNAs via the Cleavage of eIF4F and eIF3. *Mol. Cell* **16,** 575–586 (2004).

46. Kumar, G. A. & Subramaniam, K. PUF-8 facilitates homologous chromosome pairing by promoting proteasome activity during meiotic entry in C. elegans. *Dev.* **145,** (2018).

47. Xia, P., Zhou, L., Guan, J., Ding, W. & Liu, Y. Splicing factor PRP-19 regulates mitochondrial stress response. *Life Metab.* **1,** 81–93 (2022).

48. Ficociello, G. *et al.* Silencing of the mitochondrial ribosomal protein L-24 gene activates the

oxidative stress response in Caenorhabditis elegans. *Biochim. Biophys. acta. Gen. Subj.* **1867,** (2023).

49. Ryan, V. H. *et al.* Tyrosine phosphorylation regulates hnRNPA2 granule protein partitioning and reduces neurodegeneration. *EMBO J.* **40,** (2021).

50. Wang, F., Durfee, L. A. & Huibregtse, J. M. A cotranslational ubiquitination pathway for quality control of misfolded proteins. *Mol. Cell* **50,** 368–378 (2013).

51. Myers, N. *et al.* The Disordered Landscape of the 20S Proteasome Substrates Reveals Tight Association with Phase Separated Granules. *Proteomics* **18,** 1800076 (2018).

52. Tsvetkov, P. *et al.* Thermo-resistant intrinsically disordered proteins are efficient 20S proteasome substrates. *Mol. Biosyst.* **8,** 368–373 (2011).

53. Love, M. I., Huber, W. & Anders, S. Moderated estimation of fold change and dispersion for RNA-seq data with DESeq2. *Genome Biol.* **15,** 550 (2014).

54. Yanase, S., Onodera, A., Tedesco, P., Johnson, T. E. & Ishii, N. SOD-1 Deletions in Caenorhabditis elegans Alter the Localization of Intracellular Reactive Oxygen Species and Show Molecular Compensation. *Journals Gerontol. Ser. A* **64A,** 530–539 (2009).

55. Van Raamsdonk, J. M. & Hekimi, S. Superoxide dismutase is dispensable for normal animal lifespan. *Proc. Natl. Acad. Sci. U. S. A.* **109,** 5785–5790 (2012).

56. Jansen, W. T. M., Bolm, M., Balling, R., Chhatwal, G. S. & Schnabel, R. Hydrogen peroxide-mediated killing of Caenorhabditis elegans by Streptococcus pyogenes. *Infect. Immun.* **70,** 5202–5207 (2002).

57. Bolm, M., Jansen, W. T. M., Schnabel, R. & Chhatwal, G. S. Hydrogen Peroxide-Mediated Killing of Caenorhabditis elegans: A Common Feature of Different Streptococcal Species. *Infect. Immun.* **72,** 1192–1194 (2004).

58. Schiffer, J. A. *et al.* Caenorhabditis elegans processes sensory information to choose between freeloading and self-defense strategies. *Elife* **9,** 1–29 (2020).

59. Oh, K. & Kim, H. Aldicarb-induced Paralysis Assay to Determine Defects in Synaptic Transmission in Caenorhabditis elegans. *BIO-PROTOCOL* **7,** (2017).

60. Jia, Q. & Sieburth, D. Mitochondrial hydrogen peroxide positively regulates neuropeptide secretion during diet-induced activation of the oxidative stress response. *Nat. Commun. 2021 121* **12,** 1–22 (2021).

61. Zha, J., Ying, M., Alexander-Floyd, J. & Gidalevitz, T. HSP-4/BiP expression in secretory cells is regulated by a developmental program and not by the unfolded protein response. *PLoS Biol.* **17,** (2019).

62. Angeli, S. *et al.* The mitochondrial permeability transition pore activates the mitochondrial unfolded protein response and promotes aging. *Elife* **10,** (2021).

63. Kapulkin, V., Hiester, B. G. & Link, C. D. Compensatory regulation among ER chaperones in C. elegans. *FEBS Lett.* **579,** 3063–3068 (2005).

64. Shore, D. E., Carr, C. E. & Ruvkun, G. Induction of Cytoprotective Pathways Is Central to the

Extension of Lifespan Conferred by Multiple Longevity Pathways. *PLOS Genet.* **8,** e1002792 (2012).

65. Ashrafi, K. Obesity and the regulation of fat metabolism. *Wormbook* 1 (2007). doi:10.1895/WORMBOOK.1.130.1

66. Watts, J. L. Fat synthesis and adiposity regulation in Caenorhabditis elegans. *Trends Endocrinol. Metab.* **20,** 58–65 (2009).

67. Klapper, M. *et al.* Fluorescence-based fixative and vital staining of lipid droplets in Caenorhabditis elegans reveal fat stores using microscopy and flow cytometry approaches. *J. Lipid Res.* **52,** 1281 (2011).

68. Papsdorf, K. *et al.* Lipid droplets and peroxisomes are co-regulated to drive lifespan extension in response to mono-unsaturated fatty acids. *Nat. Cell Biol. 2023 255* **25,** 672–684 (2023).

69. Wang, H. *et al.* Lipin-1γ isoform is a novel lipid droplet-associated protein highly expressed in the brain. *FEBS Lett.* **585,** 1979–1984 (2011).

70. Adeyo, O. *et al.* The yeast lipin orthologue Pah1p is important for biogenesis of lipid droplets. *J. Cell Biol.* **192,** 1043–1055 (2011).

71. Zhang, P. & Reue, K. Lipin proteins and glycerolipid metabolism: Roles at the ER membrane and beyond. *Biochim. Biophys. Acta - Biomembr.* **1859,** 1583–1595 (2017).

72. Kong, J. *et al.* Spatiotemporal contact between peroxisomes and lipid droplets regulates fasting-induced lipolysis via PEX5. *Nat. Commun. 2020 111* **11,** 1–16 (2020).

73. Weller, S., Gould, S. J. & Valle, D. Peroxisome Biogenesis Disorders. *https://doi.org/10.1146/annurev.genom.4.070802.110424* **4,** 165–211 (2003).

74. Wang, Y. *et al.* Polyunsaturated fatty acids promote the rapid fusion of lipid droplets in Caenorhabditis elegans. *J. Biol. Chem.* **298,** 102179 (2022).

75. Vrablik, T. L., Petyuk, V. A., Larson, E. M., Smith, R. D. & Watts, J. L. Lipidomic and proteomic analysis of Caenorhabditis elegans lipid droplets and identification of ACS-4 as a lipid droplet-associated protein. *Biochim. Biophys. Acta - Mol. Cell Biol. Lipids* **1851,** 1337–1345 (2015).

76. Zhang, P. *et al.* Proteomic study and marker protein identification of Caenorhabditis elegans lipid droplets. *Mol. Cell. Proteomics* **11,** 317–328 (2012).

77. Ezcurra, M. *et al.* C. elegans Eats Its Own Intestine to Make Yolk Leading to Multiple Senescent Pathologies. *Curr. Biol.* **28,** 2544–2556.e5 (2018).

78. Sornda, T. *et al.* Production of YP170 Vitellogenins Promotes Intestinal Senescence in Caenorhabditis elegans. *Journals Gerontol. Ser. A Biol. Sci. Med. Sci.* **74,** 1180 (2019).

79. Kern, C. C. *et al.* C. elegans ageing is accelerated by a self-destructive reproductive programme. *Nat. Commun. 2023 141* **14,** 1–12 (2023).

80. Zhai, C. *et al.* Fusion and expansion of vitellogenin vesicles during Caenorhabditis elegans intestinal senescence. *Aging Cell* **21,** e13719 (2022).

81. Baker, M. E. Is vitellogenin an ancestor of apolipoprotein B-100 of human low-density lipoprotein and human lipoprotein lipase? *Biochem. J.* **255,** 1057 (1988).

82. Fisher, E. A. *et al.* The Degradation of Apolipoprotein B100 Is Mediated by the Ubiquitin-proteasome Pathway and Involves Heat Shock Protein 70. *J. Biol. Chem.* **272,** 20427–20434 (1997).

83. Braxton, J. R. & Southworth, D. R. Structural insights of the p97/VCP AAA+ ATPase: How adapter interactions coordinate diverse cellular functionality. *J. Biol. Chem.* **299,** 105182 (2023).

84. Takatsuki, A., Arima, K. & Tamura, G. TUNICAMYCIN, A NEW ANTIBIOTIC. I ISOLATION AND CHARACTERIZATION OF TUNICAMYCIN. *J. Antibiot. (Tokyo).* **24,** 215–223 (1971).

85. Heifetz, A., Keenan, R. W. & Elbein, A. D. Mechanism of Action of Tunicamycin on the UDP-GlcNAc:Dolichyl-Phosphate GlcNAc-1 -Phosphate Transferase. *Biochemistry* **18,** 2186–2192 (1979).

86. Long, O. S. *et al.* A C. elegans model of human α1-antitrypsin deficiency links components of the RNAi pathway to misfolded protein turnover. *Hum. Mol. Genet.* **23,** 5109–5122 (2014).

87. Ghouse, R., Chu, A., Wang, Y. & Perlmutter, D. H. Mysteries of α1-antitrypsin deficiency: emerging therapeutic strategies for a challenging disease. *Dis. Model. Mech.* **7,** 411 (2014).

88. Wang, Y. *et al.* rMATS-turbo: an efficient and flexible computational tool for alternative splicing analysis of large-scale RNA-seq data. *Nat. Protoc. 2024* 1–22 (2024). doi:10.1038/s41596-023-00944-2

89. Li, L. *et al.* An atlas of alternative polyadenylation quantitative trait loci contributing to complex trait and disease heritability. *Nat. Genet. 2021 537* **53,** 994–1005 (2021).

90. Arribere, J. A., Kuroyanagi, H. & Hundley, H. A. mRNA Editing, Processing and Quality Control in Caenorhabditis elegans. *Genetics* **215,** 531–568 (2020).

91. Tourasse, N. J., Millet, J. R. M. & Dupuy, D. Quantitative RNA-seq meta-analysis of alternative exon usage in C. elegans. *Genome Res.* **27,** 2120–2128 (2017).

92. Matsushita-Ishiodori, Y., Yamanaka, K. & Ogura, T. The C. elegans homologue of the spastic paraplegia protein, spastin, disassembles microtubules. *Biochem. Biophys. Res. Commun.* **359,** 157–162 (2007).

93. Matsushita-Ishiodori, Y., Yamanaka, K., Hashimoto, H., Esaki, M. & Ogura, T. Conserved aromatic and basic amino acid residues in the pore region of Caenorhabditis elegans spastin play critical roles in microtubule severing. *Genes to Cells* **14,** 925–940 (2009).

94. Plaud, C. *et al.* Functional differences of short and long isoforms of spastin harboring missense mutation. *DMM Dis. Model. Mech.* **11,** (2018).

95. Evans, R. *et al.* Protein complex prediction with AlphaFold-Multimer. *bioRxiv* 2021.10.04.463034 (2022). doi:10.1101/2021.10.04.463034

96. Chang, C. L. *et al.* Spastin tethers lipid droplets to peroxisomes and directs fatty acid trafficking through ESCRT-III. *J. Cell Biol.* **218,** 2583–2599 (2019).

97. Papadopoulos, C. *et al.* Spastin Binds to Lipid Droplets and Affects Lipid Metabolism. *PLOS Genet.* **11,** e1005149 (2015).

98. Koyuncu, S. *et al.* Rewiring of the ubiquitinated proteome determines ageing in C. elegans. *Nat. 2021 5967871* **596,** 285–290 (2021).

99. Larance, M. *et al.* Global Proteomics Analysis of the Response to Starvation in C. elegans*. *Mol. Cell. Proteomics* **14,** 1989–2001 (2015).

100. Sladowska, M. *et al.* Proteasome activity contributes to pro-survival response upon mild mitochondrial stress in Caenorhabditis elegans. *PLOS Biol.* **19,** e3001302 (2021).

101. Zhou, Y. *et al.* Metascape provides a biologist-oriented resource for the analysis of systems-level datasets. *Nat. Commun.* **10,** 1–10 (2019).

102. Bajorek, M., Finley, D. & Glickman, M. H. Proteasome disassembly and downregulation is correlated with viability during stationary phase. *Curr. Biol.* **13,** 1140–1144 (2003).

103. Choi, W. H. *et al.* Open-gate mutants of the mammalian proteasome show enhanced ubiquitin-conjugate degradation. *Nat. Commun. 2016 71* **7,** 1–12 (2016).

104. Weingarten, M. D., Lockwood, A. H., Hwo, S. Y. & Kirschner, M. W. A protein factor essential for microtubule assembly. *Proc. Natl. Acad. Sci.* **72,** 1858–1862 (1975).

105. Weinreb, P. H., Zhen, W., Poon, A. W., Conway, K. A. & Lansbury, P. T. NACP, a protein implicated in Alzheimer's disease and learning, is natively unfolded. *Biochemistry* **35,** 13709–13715 (1996).

106. Kepchia, D. *et al.* Diverse proteins aggregate in mild cognitive impairment and Alzheimer's disease brain. *Alzheimer's Res. Ther.* **12,** 1–20 (2020).

107. Miao, J. *et al.* Pathological Tau From Alzheimer's Brain Induces Site-Specific Hyperphosphorylation and SDS- and Reducing Agent-Resistant Aggregation of Tau in vivo. *Front. Aging Neurosci.* **11,** 34 (2019).

108. Mutlu, A. S., Duffy, J. & Wang, M. C. Lipid metabolism and lipid signals in aging and longevity. *Dev. Cell* **56,** 1394–1407 (2021).

109. Heimbucher, T., Hog, J., Gupta, P. & Murphy, C. T. PQM-1 controls hypoxic survival via regulation of lipid metabolism. *Nat. Commun. 2020 111* **11,** 1–15 (2020).

110. Cipolla, C. M. & Lodhi, I. J. Peroxisomal Dysfunction in Age-Related Diseases. *Trends Endocrinol. Metab.* **28,** 297–308 (2017).

111. Kou, J. *et al.* Peroxisomal alterations in Alzheimer's disease. *Acta Neuropathol.* **122,** 271–283 (2011).

112. Rhee, S. G., Woo, H. A., Kil, I. S. & Bae, S. H. Peroxiredoxin Functions as a Peroxidase and a Regulator and Sensor of Local Peroxides. *J. Biol. Chem.* **287,** 4403–4410 (2012).

113. Zhu, B. *et al.* ER-associated degradation regulates Alzheimer's amyloid pathology and memory function by modulating γ-secretase activity. *Nat. Commun. 2017 81* **8,** 1–15 (2017).

114. Stojkovska, I. *et al.* Rescue of α-synuclein aggregation in Parkinson's patient neurons by

synergistic enhancement of ER proteostasis and protein trafficking. *Neuron* **110,** 436–451.e11 (2022).

115. Sornda, T. *et al.* Production of YP170 Vitellogenins Promotes Intestinal Senescence in Caenorhabditis elegans. *Journals Gerontol. Ser. A* **74,** 1180–1188 (2019).

116. Singh, J. & Aballay, A. Endoplasmic Reticulum Stress Caused by Lipoprotein Accumulation Suppresses Immunity against Bacterial Pathogens and Contributes to Immunosenescence. *MBio* **8,** (2017).

117. Liao, W., Yeung, S. C. J. & Chan, L. Proteasome-mediated Degradation of Apolipoprotein B Targets Both Nascent Peptides Cotranslationally Before Translocation and Full-length Apolipoprotein B After Translocation into the Endoplasmic Reticulum. *J. Biol. Chem.* **273,** 27225–27230 (1998).

118. Brenner, S. THE GENETICS OF CAENORHABDITIS ELEGANS. *Genetics* **77,** 71–94 (1974).

119. Phipson, B., Lee, S., Majewski, I. J., Alexander, W. S. & Smyth, G. K. Robust hyperparameter estimation protects against hypervariable genes and improves power to detect differential expression. *https://doi.org/10.1214/16-AOAS920* **10,** 946–963 (2016).

120. Kim, D., Langmead, B. & Salzberg, S. L. HISAT: A fast spliced aligner with low memory requirements. *Nat. Methods* **12,** 357–360 (2015).

121. Liao, Y., Smyth, G. K. & Shi, W. Sequence analysis featureCounts: an efficient general purpose program for assigning sequence reads to genomic features. **30,** 923–930 (2014).

122. Wu, T. *et al.* clusterProfiler 4.0: A universal enrichment tool for interpreting omics data. *Innov.* **2,** 100141 (2021).

123. Karunarathne, P., Pocquet, N., Labbé, P. & Milesi, P. BioRssay: an R package for analyses of bioassays and probit graphs. *Parasites and Vectors* **15,** 1–6 (2022).

124. Gusarov, I. *et al.* Dietary thiols accelerate aging of C. elegans. *Nat. Commun. 2021 121* **12,** 1–14 (2021).

125. Wang, F. Y. & Ching, T. T. Oil Red O staining for lipid content in Caenorhabditis elegans. *Bio-protocol* **11,** (2021).

126. Na, H. *et al.* Identification of lipid droplet structure-like/resident proteins in Caenorhabditis elegans. *Biochim. Biophys. Acta - Mol. Cell Res.* **1853,** 2481–2491 (2015).